Extracting olivine (Fo–Fa) compositions from Raman spectral peak positions

Karla E. Kuebler [*], Bradley L. Jolliff, Alian Wang, Larry A. Haskin

Department of Earth and Planetary Sciences and the McDonnell Center for Space Sciences, Washington University, St. Louis, MO 63130, USA

Received 6 February 2006; accepted in revised form 21 July 2006

Abstract

The dominant feature of the olivine Raman spectrum is a doublet that occurs in the spectral region of 815–825 cm^{-1} (DB1) and 838–857 cm^{-1} (DB2). These features arise from coupled symmetric and asymmetric stretching vibrational modes of the constituent SiO_4 tetrahedra. The frequencies of both peaks show monotonic shifts following cation substitution between forsterite and fayalite. We present a calibration for extracting olivine Fo contents (Fo = Mg/(Mg + Fe) molar ratio; Fo_{0-100}) from the peak positions of this doublet, permitting estimates of chemical composition from Raman spectra (acquired in the laboratory or field) as well as providing information on crystal structure (distinction of polymorphs). Eight samples spanning the compositional range from forsterite to fayalite were used to develop the calibration equations for the DB1 and DB2 peaks individually and together. The data indicate that the DB1 peak is more reliable for calculating the compositions of Fe-rich olivine but that the DB2 peak is better for magnesian compositions. The two-peak calibration overcomes the limitations of the single-peak calibrations and is capable of calculating olivine compositions to within ±10 Fo units.

© 2006 Elsevier Inc. All rights reserved.

1. Introduction

Laser Raman spectroscopy is a powerful method for structural and compositional characterization of minerals. Raman spectra of most minerals and organic compounds have sharp, well-separated spectral peaks that facilitate phase identifications directly from raw spectra of mixtures (rocks and soils). Raman spectral patterns (number of peaks and their relative intensities) and the positions of major Raman peaks are determined by fundamental vibrational modes of chemical bonds having a high degree of covalence in their structure, such as the SiO_4 anionic group in silicates (SO_4 in sulfates, PO_4 in phosphates, and CO_3 in carbonates). Compared to infrared spectra, Raman peaks from overtones and combination vibrational modes are generally much weaker than those of the fundamental modes, reducing the complexity of the spectrum. The properties of strong metallic ions (Fe, Mg, Ca) within the structure are commonly expressed by the wavenumber shift of the major Raman peaks of stronger covalent groups (e.g., SiO_4) because these metallic ions share the coordinating oxygen with Si (or S, P, C) and the difference in atomic masses and attractive forces between the Fe, Mg, Ca and oxygen affect the vibrational frequencies of Si–O bonds. In minerals that exhibit cation substitutions (e.g., olivine, pyroxene), major Raman peak positions undergo systematic and measurable peak shifts. Such peak shifts can be used to calculate the ratios of the cations involved (e.g., Mg/(Mg + Fe) in olivine, Mg/(Mg + Fe + Ca) in pyroxene) and further address the geochemical conditions during formation and throughout crystallization history (Wang et al., 1995, 1999, 2001, 2004a; Haskin et al., 1997; Mernagh and Hoatson, 1997).

Motivation for this type of study stems from work in recent years to develop the technology and methodology of microbeam Raman spectroscopy for in-situ planetary surface exploration (Wang et al., 1995, 2003a, 2004a; Haskin

---

[*] Corresponding author. Fax: +1 314 935 7361.

E-mail address: kuebler@levee.wustl.edu (K.E. Kuebler).

et al., 1997). We are obtaining laser Raman spectra of the major rock-forming mineral groups (pyroxene, feldspar, Fe–Ti–Cr-oxides, carbonates and sulfates, Wang et al., 2001, 2004a, 2005; Freeman et al., 2003) with the anticipation that spectra obtained from a remotely deployed Raman spectrometer on the surface of another planet might be used to determine mineralogy, provide information regarding mineral chemistry, and aid lithologic distinction. Toward that end, the Mars Microbeam Raman Spectrometer (MMRS) was developed for in situ mineralogic characterization on the surface of Mars (Wang et al., 2003b).

There is a strong scientific desire in planetary exploration for an instrument capable of extracting mineralogic and compositional information from stand-alone measurements, such as laser Raman spectroscopy is capable of providing. The α-particle X-ray Spectrometer (APXS) that has been used in recent Mars exploration missions will also be used in future, near-term planetary-surface exploration. The APXS provides chemical compositions for bulk rock or soil samples from which mineralogy can be inferred. However, no instruments currently planned for flight are able to determine the chemical composition of individual mineral grains in situ, which would provide improved constraints on mineral assemblages, rock lithology, and petrologic relationships. Microbeam detection combined with linear scanning is one of the central design concepts of the MMRS (Haskin et al., 1997). This operational approach takes hundreds of spectra in a stepwise fashion along a linear traverse (i.e., a point count) on the surface of a rock (or soil) sample. Each spectrum, produced by microbeam excitation of a spot <20 μm in diameter, reflects contributions from only one or a few mineral grains. Structural information is available from the pattern of peaks present in the spectrum and cation ratios can be calculated from the Raman peak positions of minerals showing cation substitution. Therefore, chemical and structural information are both embedded in the Raman spectra of minerals. Even though such compositions are not as precise as those determined by electron microprobe analysis (EMPA), one hundred Raman spectra with such paired information from a geologic target (rock or soil) on other planet would be extremely valuable from the point of view of science and mission operations.

A calibration that quantitatively links the Raman peak positions of a set of solid-solution minerals (olivine, in this study) to a specific cation ratio (Mg/(Mg + Fe) for Mg- and Fe-olivine) is essential for extracting mineral chemistry from remotely acquired Raman spectra. Previously, we developed a calibration for calculating Mg/(Mg + Fe + Ca) and Ca/(Mg + Fe + Ca) cation ratios in pyroxene based on co-registered Raman and EMP analyses of a set of pyroxene grains within two lunar samples (15273,7039 and 14161,7080). This calibration was tested against a set of similar data for the pyroxene grains in martian meteorite EETA 79001, and achieved an accuracy of ±10% in calculating the Mg/(Mg + Fe + Ca) ratio, with a slightly larger uncertainty for the Ca/(Mg + Fe +

Ca) ratio calculation (Wang et al., 2001). We have observed similar Raman peak position shifts in chromite (Al, Fe, Cr cation substitution), ilmenite (Fe, Ti), and hematite (Fe, Ti) (Wang et al., 2004a), and smaller shifts in feldspar (Na, K, Ca) (Freeman et al., 2003). The step-by-step RAMANITA calibration method of Smith (2005) is conceptually similar but mathematically generalized and appears to be better suited to the study of multivariate mineral systems, such as garnet and amphiboles, in which several substitutions may occur.

Mineral chemistry determined from remotely acquired Raman spectra can be used to constrain the petrologic characteristics of a given rock or soil sample (Wang et al., 1999, 2004b; Kuebler et al., 2002). Sequences of spectra can be used to estimate grain sizes and the compositional zoning of minerals. Histograms of Raman-derived cation ratios produced from a point count illustrate the range of mineral compositions present in a sample, the complexity of which supplies information about a rock's cooling history (Wang et al., 1999, 2004b). Information of this sort will aid the interpretation of sample crystallization and differentiation histories and help discriminate lithologies in a suite of samples.

A Raman spectroscopic study of martian meteorite EETA 79001 (Wang et al., 2004b) used a preliminary calibration to calculate Mg/(Mg + Fe) in olivine, developed from the data of Guyot et al. (1986) and Chopelas (1991), together with the pyroxene calibration developed by Wang et al. (2001). The current paper presents a new calibration to extract the Mg/(Mg + Fe) ratio of olivine from Raman peak positions based on a set of co-registered Raman and EMP measurements on eight lunar, martian, and terrestrial olivine samples (all those listed in Table 1 except LAP 02224,24 and Finch-Robie). This new calibration enables the estimation of olivine cation ratios at higher accuracy and precision than before, and will improve in situ sample characterization capabilities.

2. Analytical methods and registration of Raman and EMP analyses

Co-registered Raman and EMP analyses were made at the same locations in each olivine grain to correlate the Raman peak positions and chemical compositions precisely. Co-registered analyses were made at a few to over twenty spots on each sample; the locations of all Raman spectra were photographed and the photos used along with microscopic features to locate the subsequent EMP analyses. The only calibration samples for which co-registered EMP analyses were not taken are the synthetic end members, which are electron microprobe standards. Instead, we use the accepted compositions of these two samples to correspond with all of the Raman spectra acquired from them. We also do not have corresponding EMP data for the point count data from the rock chips of martian meteorite EETA 79001 (low signal-to-noise spectra used to test the calibration, but not in its creation). We compare these Raman

Table 1
List of samples used to create and test the olivine calibration

Sample/location	Type of sample	Source	Previous studies, Raman or EMPA
Fayalite 203	Synthetic, HUPS 401	WU EMP lab	Takei (1978)
Finch-Robie	Synthetic	A. Hofmeister	
Forsyth Iron Mine, Hull, Quebec, Canada	Magnetite bearing iron ore	A. Hofmeister	Jambor et al. (2002); Hogarth (1983)
Rustenberg, Transvaal, South Africa	Hortonolite	A. Hofmeister	
LAP02224,24	Lunar meteorite, basalt paired with LAP02205	NASA, JSC Meteorite Curatorial Facility	Zeigler et al. (2005) Korotev et al. (2002); McBride et al. (2004a)
NWA 773	Lunar meteorite, breccia, olivine gabbro lithology	NASA, JSC Meteorite Curatorial Facility	Jolliff et al. (2003); Korotev et al. (2002) Fagan et al. (2003); Bridges et al. (2002)
EETA79001,530	SNC meteorite, basaltic shergottite, xenocrysts	NASA, JSC Meteorite Curatorial Facility	Wang et al. (2004a,b); Steele and Smith (1982) McSween and Jarosewich (1983); Meyer (1996)
San Carlos, Arizona, USA	Large polished forsterite grain	A. Hofmeister	Frey and Prinz (1978); Galer and O'nions (1989); Guyot et al. (1986)
Twin Sisters Range, Washington, USA	Dunite	Burminco (#1390-A)	Christensen (2002)
Forsterite 204	Synthetic, HUPS 433	WU EMP lab	Takei and Kobayashi (1974); Ishii (1978); Guyot et al. (1986)

data to the published EMP analyses of McSween and Jarosewich (1983) and Steele and Smith (1982).

All of the Raman spectra used to develop the calibration data were collected on a HoloLab 5000[®] spectrometer (Kaiser Optical Systems, Inc.). The 532.3 nm line from a frequency-doubled Nd:YAG laser was used as the excitation source, which produces an unpolarized, condensed beam ∼6 μm diameter at the sample, with an average power of 15 mW. All of the spectra were acquired using a 20× long-working distance objective (0.4 NA) and spectral accumulation time of 30 s. The olivine samples used for calibration are generally coarse-grained and well crystallized (or synthetic) and do not suffer from any laser heating effects at this laser power. Similarly, Chopelas (1991) observed no line broadening of forsterite peaks with a 433 nm laser at 20–200 mW, but did observe signs of laser heating in fayalite spectra at powers >20 mW.

The HoloLab 5000[®] is a holographic grating spectrometer that covers the −60 to +4370 cm^{-1} Stokes shifted Raman region relative to the laser wavelength. The grating separates this spectral region into two segments on the face of a 1024 × 256 pixel CCD camera with a 200 cm^{-1} overlap between spectral segments, providing a dispersion of 2.07 cm^{-1} per camera pixel. The absolute wavelength scale of the CCD camera is calibrated using the standard emission lines of a neon arc lamp. The Holograms[®] software uses a cubic spline routine to smooth the spectra acquired from the camera and fit it with a 3rd order polynomial. The resulting calibration curve has a standard deviation of error of 0.003 nm/pixel. The spectral resolution of this camera is 3 pixels or 6.2 cm^{-1}. The absolute frequency of the Nd:YAG laser shows slight daily variations, which are corrected according to the measured Raman shift of a single-crystal silicon standard to the standard value of 520.5 cm^{-1}. Measurements of the Raman shifts of other Raman standard materials such as cyclohexane, polystyrene, etc. show that this Raman system can measure

Raman peak positions with an accuracy of ±0.5 cm^{-1} and a precision of ±0.1 cm^{-1}.

The Raman point-count data (on martian meteorite EETA 79001 rock chips 476 and 482) used in the discussion of this paper, were collected on the same instrument but using the 632.8 nm line of a He–Ne laser, and similar operating conditions, i.e., 20× objective (0.4 numerical aperture (NA)) and 10–80 s accumulation times, corrected to a Si wafer shift of 520.5 cm^{-1}. All Raman peak-position values were obtained by spectral deconvolution using a least-squares fitting subroutine of the Grams 32™ software package with a mixed Gaussian–Lorentzian peak shape, linear baseline, and the constraint-free iteration option for fitting all parameters until convergence (or a minimum) was attained.

The EMP data were collected on a JEOL 733 Superprobe with three wavelength-dispersive spectrometers, back-scattered electron (BSE) detector, and Advanced Microbeam™ automation. The accelerating voltage was 15 kV and the nominal beam current 30 nA. We used a broad electron beam (10 μm) to obtain the average composition of the analyzed area and better approximate the area sampled by the Raman laser beam (∼6 μm diameter). The EMP routine used a combination of silicate and oxide standards, and analyzed for Si, Al, Ti, V, Cr, Fe, Mn, Mg, Zn, Ca, and Ni. X-ray matrix corrections were made using a modified CITZAF routine (Armstrong, 1988) incorporated into the electron microprobe software.

Discrepancies occur within the co-registered data set despite photo-documentation and compensation for location errors using broad electron-beam analysis. One explanation is the difference in the volume from which Raman photons are collected vs. the volume X-rays are collected from during EMP analysis. This difference is caused by the different penetration depths of the laser vs. the electron beam. A laser of 532 nm has a bright green color and its penetration depth depends on the color and the transparency of

the sample. Penetration can be on the order of millimeters in an Mg-end member olivine (forsterite, light yellow-green), but is much shallower (μm scale) in a Fe-end member olivine (fayalite, black). The electron beam penetration is on the order of a few micrometers in all samples. In zoned olivine, the difference in sample volumes may produce a discrepancy between the cation ratio derived from Raman analyses and that from EMP analyses. Making multiple Raman and EMP measurements on the same olivine grain helps average out the zoning effect, but does not totally remove it. This is one of our motives for using averaged values (Raman peak positions and compositions) to produce the calibration.

3. Olivine samples and the Raman spectrum of olivine

We use a combination of four terrestrial and two meteorite samples plus two synthetic end member olivine grains to cover the entire range of Mg, Fe-olivine compositions between forsterite and fayalite (Fo = Mg/(Mg + Fe) molar ratio; Fo_0–Fo_{100}, Table 1) in the calibration. Only samples showing little or no chemical zoning were used to develop the calibration, along with the data from one modestly zoned olivine sample (EETA 79001). The average chemical compositions and the average Raman spectral peak positions used to create the calibration data set are given in Tables 2 and 3. The "calibration" data set also includes the extreme EMP data points from EETA 79001 and the extreme Raman peak positions of the Hortonolite sample. This produced a total of 12 paired Raman and EMP data points. The "full" data set is also used to assess the calibration; this consists of the 83 individual data points from which the calibration data set was created plus three spectra from strongly zoned olivine in a third meteorite, LAP 02224,24 (data included in Tables 2 and 3 but not used in the calibration data set). These two data sets are described in more detail later. A brief description of the geologic occurrence, co-existing mineral phases, and the textural and chemical features of olivine grains in each sample are provided in the Appendix A.

Olivine is an orthosilicate of orthorhombic *Pbnm* structure (forsterite: $a = 4.75$, $b = 10.20$, $c = 5.98$ Å; fayalite: $a = 4.82$, $b = 10.48$, $c = 6.09$ Å) with complete solid solution between the Fe and Mg-end members (Papike, 1987). Typically, there is little substitution; Mn and Ca are observed in Fe-rich olivine, whereas Ni and Cr^{3+} are more common in Mg-rich olivine. Other minor elements include Al, Ti, and Fe^{3+}, although Fe^{3+} may result primarily from magnetite inclusions in oxidized samples (Deer et al., 1992).

The structure of olivine consists of isolated SiO_4 tetrahedra with each of the tetrahedral oxygen shared by three octahedral cations. Oxygen atoms form approximate hexagonal closest packing, with half of the available octahedral sites occupied by Mg^{2+} and/or Fe^{2+}. These octahedra form serrated chains and layers, that are staggered perpendicular to the *a* axis by a *b*/2 translation along the *b*-axis (Papike, 1987). There are two distinct types of octahedra in the olivine structure (Fig. 1); M1 are located at centers of symmetry ($\bar{1}$) and M2 are located on mirror planes (m). M1 octahedra have a shorter average M–O bond length (2.094 and 2.161 Å for forsterite and fayalite, respectively, Smyth and Bish, 1988) and a more regular shape than M2 (2.129 and 2.177 Å). All corner oxygen atoms in the SiO_4 tetrahedra are shared with octahedra, but only some edges are shared. The combination of these linkages and the small ionic radius of the octahedral cations distort the SiO_4 tetrahedra relative to the ideal tetrahedral form. SiO_4 tetrahedra in olivine are elongated into trigonal pyramids along the *a*-axis while the shared edges of the M1 and M2 octahedra are shortened relative to their unshared edges (Papike, 1987). The degree of SiO_4 distortion is higher in forsterite (Quadratic Elongation 1.0122, Angle Variance 49.4, Smyth and Bish, 1988)[1] than in fayalite (Quadratic Elongation 1.0085, Angle Variance 36.7), which is also reflected in the length variations of the Si–O bonds in the SiO_4 tetrahedra: from 1.6139 to 1.6549 Å ($\Delta = 0.0410$) in forsterite and from 1.6248 to 1.6533 Å ($\Delta = 0.0285$) in fayalite. Because the ionic radius of $^{(VI)}Fe^{2+}$ (0.86 Å, high spin state, Whittaker and Muntus, 1970) is larger than that of Mg^{2+} (0.80 Å) the M1 and M2 octahedra of fayalite are more similar than those of forsterite; the volume difference between the two octahedra in fayalite is only half of that of forsterite (Smyth and Bish, 1988).

Because of its importance in terrestrial mantle research, olivine is well studied, both by infrared spectroscopy and by Raman spectroscopy (Pâques-Ledent and Tarte, 1973; Ishii, 1978; Piriou and McMillan, 1983; Guyot et al., 1986; Hofmeister, 1987; Lam et al., 1990; Chopelas, 1991; Hofmeister and Chopelas, 1991; Mohanan et al., 1993). Most of this research, however, is focused on peak assignments and changes in the olivine crystal structure with regard to physical properties where composition is known. These Raman peak assignments form the scientific basis for the creation of this calibration.

Detailed peak assignments of the polarized Raman spectrum of forsterite can be found in Ishii (1978); Price et al. (1987); Piriou and McMillan (1983) and McMillan (1985), and those of olivine in general are given by Chopelas (1991). Olivine has 84 normal vibrational modes; among which, 81 are optic modes and 36 are Raman-active modes (Ishii, 1978; Hofmeister, 1987). A Raman spectrum of olivine (forsterite and fayalite in Fig. 2) can be reasonably divided into three spectral regions: $<400\ cm^{-1}$, 400–$700\ cm^{-1}$, and 700–$1100\ cm^{-1}$.

---

[1] Quadratic elongation and angle variance are both measures of distortion used to describe tetrahedra and octahedra. Quadratic elongation is defined as a unitless measure of distortion, reflecting both angular and distance distortions. Angle variance is a measure of the variance of the central angle of tetrahedra/octahedra and has units of degrees squared (Smyth and Bish, 1988).

Table 2
Average compositions of the olivine calibration standards and LAP02224,24 by EMPA

	LAP02224,24		Forsyth Mine		Hortonolite				NWA773		EETA 79001,530				San Carlos		Twin	Fa 203[b]	Fo 204
	av. $n=3$	SD	av. $n=2$	SD	low DB2 $n=1$	av. $n=16$	SD	high DB2 $n=1$	av. $n=23$	SD	rim $n=1$	av. $n=9$	SD	core $n=1$	av. $n=2$	SD	Sisters $n=1$	Published value	Published value
FeO^c	51.47	5.90	65.64	0.47	47.87	48.02	0.35	48.34	30.47	1.46	36.45	32.19	3.47	27.53	10.63	0.05	8.58	70.22	
MgO	14.96	4.80	3.32	0.08	18.23	17.99	0.31	17.89	32.26	1.33	26.54	30.44	3.07	35.20	48.57	0.17	48.96	0.24	57.30
Cr_2O_3	<0.11	0.04	<0.11	0.03	<0.11	<0.11	0.02	<0.11	<0.11	0.03	<0.11	<0.11	0.09	<0.11	<0.11	0.03	<0.11		
TiO_2	<0.06	0.03	<0.06	0.00	<0.06	<0.06	0.03	<0.06	<0.06	0.02	<0.06	<0.06	0.01	<0.06	<0.06	0.02	<0.06		
MnO	0.48	0.09	0.94	0.04	0.61	0.63	0.05	0.62	0.33	0.05	0.63	0.60	0.06	0.59	0.18	0.02	0.12		
V_2O_3	<0.19	0.01	<0.19	0.01	<0.19	<0.19	0.02	<0.19	<0.19	0.01	<0.19	<0.19	0.03	<0.19	<0.19	0.03	<0.19		
Al_2O_3	<0.04	0.00	<0.04	0.00	<0.04	<0.04	0.00	<0.04	<0.04	0.02	<0.04	0.10	0.22	<0.04	<0.04	0.01	<0.04		
CaO	0.42	0.02	<0.03	0.01	0.07	0.05	0.02	0.06	0.23	0.05	0.26	0.24	0.02	0.22	0.07	0.00	<0.03		
ZnO	<0.17	0.00	<0.17	0.03	<0.17	<0.17	0.05	<0.17	<0.17	0.04	<0.17	<0.17	0.02	<0.17	<0.17	0.01	<0.17		
SiO_2	32.76	0.95	29.62	0.07	33.49	33.30	0.35	33.76	36.54	0.28	35.22	36.04	0.75	37.26	40.29	0.71	41.37	29.54	42.70
NiO	<0.07	0.01	<0.07	0.01	<0.07	0.08	0.03	0.09	<0.07	0.02	<0.07	<0.07	0.02	0.08	0.30	0.00	0.35		
Totals	100.2		99.6		100.4	100.2		100.8	100.0		99.2	99.7		100.29	100.2		99.4	100.0	100.0
Number of ions based on 4 oxygens																			
Si	0.994	0.002	0.988	0.004	0.993	0.992	0.006	0.998	0.992	0.401	0.996	0.991	0.006	0.988	0.992	0.007	1.013	1.000	1.000
Al	0.000	0.000	0.000	0.000	0.000	0.000	0.000	0.000	0.000	0.018	0.001	0.003	0.007	0.001	0.000	0.000	0.000	0.000	0.000
Ti	0.001	0.001	0.000	0.000	0.000	0.000	0.001	0.000	0.001	0.018	0.000	0.000	0.000	0.000	0.000	0.000	0.000	0.000	0.000
V	0.000	0.000	0.000	0.000	0.000	0.000	0.000	0.000	0.000	0.019	0.000	0.000	0.001	0.000	0.000	0.001	0.000	0.000	0.000
Cr	0.001	0.001	0.001	0.001	0.000	0.000	0.000	0.001	0.001	0.018	0.000	0.001	0.002	0.001	0.002	0.001	0.001	0.000	0.000
Fe^{2+}	1.306	0.188	1.830	0.010	1.187	1.196	0.009	1.195	0.692	0.262	0.862	0.740	0.096	0.610	0.219	0.003	0.176	1.988	0.000
Mn^{2+}	0.012	0.003	0.027	0.001	0.015	0.016	0.001	0.015	0.008	0.016	0.015	0.014	0.001	0.013	0.004	0.000	0.002	0.000	0.000
Mg	0.677	0.194	0.165	0.004	0.806	0.799	0.015	0.788	1.305	0.528	1.119	1.248	0.098	1.391	1.782	0.012	1.787	0.012	2.000
Zn	0.000	0.000	0.000	0.000	0.001	0.001	0.001	0.000	0.001	0.018	0.001	0.001	0.000	0.000	0.000	0.000	0.000	0.000	0.000
Ca	0.014	0.001	0.001	0.000	0.002	0.002	0.001	0.002	0.007	0.016	0.008	0.007	0.001	0.006	0.002	0.000	0.000	0.000	0.000
Ni	0.000	0.000	0.000	0.000	0.001	0.002	0.001	0.002	0.001	0.018	0.001	0.001	0.000	0.002	0.006	0.000	0.007	0.000	0.000
Sum oct	2.011		2.024		2.013	2.016		2.004	2.015		2.007	2.015		2.024	2.015		1.974	2.000	2.000
Sum tet	0.994		0.988		0.993	0.992		0.998	0.992		0.996	0.991		0.988	0.992		1.013	1.000	1.000
Total	3.005		3.012		3.006	3.007		3.002	3.007		3.003	3.006		3.012	3.007		2.987	3.000	3.000
Fo^a	**0.34**	0.097	**0.08**	0.002	**0.40**	**0.40**	0.006	**0.39**	**0.65**	0.268	**0.56**	**0.62**	0.048	**0.69**	**0.089**	0.001	**0.91**	**0.01**	**0.00**

[a] Mn^{2+} included with Fe^{2+} when calculating Fo, Fo = Mg/(Mg + Fe + Mn) molar × 100.
[b] MgO not reported in published analysis, value from in-house analyses.
[c] All Fe assumed to be Fe^{2+}.

Table 3
Olivine doublet peak positions of the calibration data set and LAP02224,24

	Fayalite 203	Forsyth	LAP 02224,24	Rustenburg Hortonolite			EETA79001,530			NWA773	San Carlos	Twin Sisters	Forsterite 204
	av. n = 15	av. n = 2	av. n = 3	low DB2 n = 1	av. n = 16	high DB2 n = 1	rim n = 1	av. n = 9	core n = 1	av. n = 23	av. n = 2	av. n = 1	av. n = 15
DB1	815.0	815.3	816.2	817.1	817.0	816.5	818.2	819.0	819.6	819.0	822.5	823.1	824.7
SD[a]	0.09	0.07	0.29	0.00	0.26	0.03	0.05	0.54	0.06	0.16	0.01	0.00	0.03
DB2	838.8	837.4	840.7	842.8	843.2	844.4	847.6	848.7	849.9	849.2	854.5	855.0	856.7
SD	0.52	1.18	1.17	0.00	0.54	0.03	0.03	0.90	0.01	0.26	0.05	0.00	0.02

[a] Standard deviations used when n = 1 come from replicate curve fitting analyses of the same spectrum.
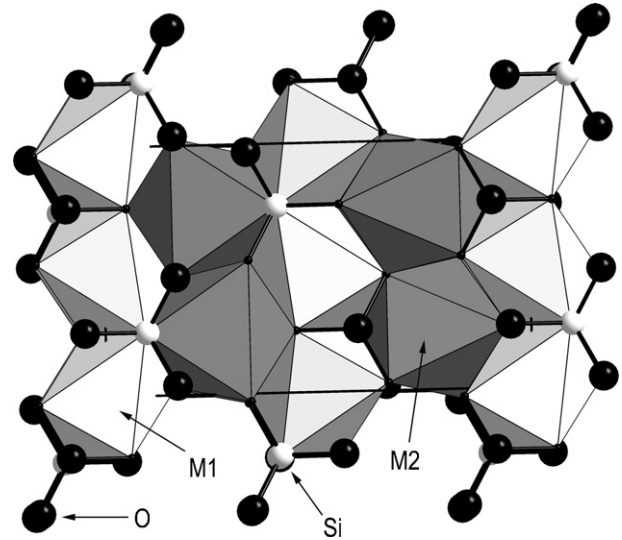
Fig. 1. Olivine (*Pbnm*) crystal structure with isolated SiO_4 tetrahedra linked by M1 and M2 octahedral cations, viewed down the *a* axis. Each oxygen is linked to three octahedral cations (Mg or Fe) distorting both the octahedra and tetrahedra. The major features of the Raman spectrum of olivine arise from symmetric and asymmetric vibrations of the tetrahedra whose frequencies are damped with respect to the masses of the cations present. Structure drawing made using the Diamond™ software.

Peaks between 700 and 1100 cm^{-1} are attributed to the internal stretching vibrational modes of the SiO_4 ionic group. The dominant feature of the olivine spectrum is a doublet in this region with peaks near 820 cm^{-1} and
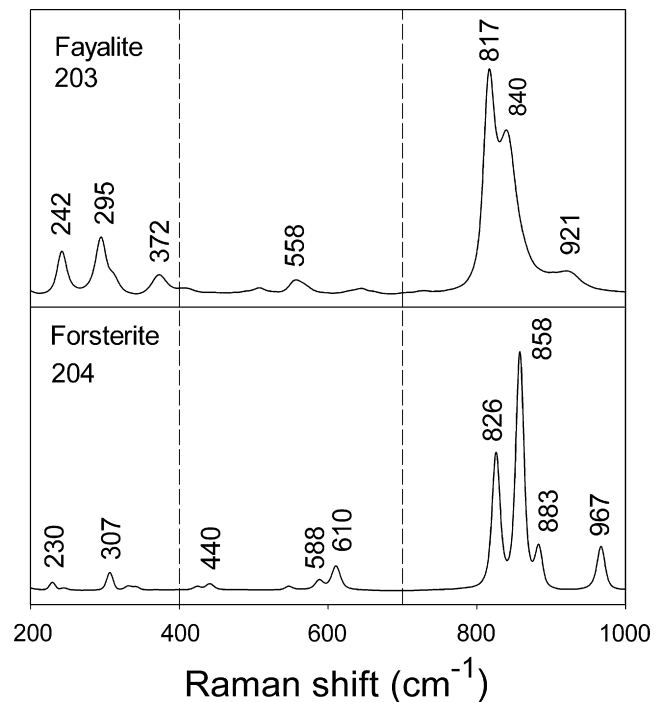

Fig. 2. Spectra of the synthetic olivine end members fayalite and forsterite. The peak near 820 cm^{-1} is referred to as DB1 in the text and the peak near 850 cm^{-1} is referred to as DB2.

850 cm^{-1} whose relative peak heights are a function of crystal orientation (Ishii, 1978; Chopelas, 1991). These peaks are the most characteristic olivine peaks and are most frequently used to identify olivine in the multi-phase spectra from igneous materials, i.e., rocks and soils derived from igneous rocks (Wang et al., 1995, 2004b).

Peaks in the 400–700 cm^{-1} spectral region result from internal bending vibrational modes of the SiO$_4$ ionic groups. Peaks below 400 cm^{-1} are assigned to lattice modes: rotational and translational motions of SiO$_4$ as a unit, and translational motions of octahedral cations (Mg^{2+}, Fe^{2+}) in the crystal lattice (Chopelas, 1991). The peaks in these two regions are normally much weaker than those in the 700–1100 cm^{-1} region, and not often resolved in multi-phase spectra from mixtures. Therefore, only the peak positions of the doublet in the 700–1100 cm^{-1} region were analyzed in this study to develop the olivine calibration.

We address the limitations of the olivine calibration with respect to mineral zoning, signal-to-noise ratios (since rock spectra frequently have less than optimal S/N), and peak resolution, which depends on relative peak heights as well as peak separation. Because the ranges in peak position are so broad, we refer to the shorter wavelength peak of the olivine doublet as DB1 (doublet peak #1, the peak in the 815–825 cm^{-1} region) and the longer wavelength peak as DB2 (doublet peak #2, the peak in the 838–857 cm^{-1} region) to discuss variations in the spectra from fayalite to forsterite.

The peak positions of the olivine doublet are observed to vary with composition (Fig. 3) across the continuum of Mg/(Mg + Fe) (Fo ranging from 0 to 100) compositions, the observed range of peak positions for the DB1 peak is ∼10 wavenumbers: from 815.0 cm^{-1} in the fayalite spectrum to 824.8 cm^{-1} in the forsterite spectrum. The observed range for the DB2 peak is wider, ∼20 wavenumbers: from 837.8 cm^{-1} in fayalite to 856.7 cm^{-1} in forsterite. The systematic peak-position shift towards higher wavenumbers with increasing Fo content is linked to the decrease of atomic mass and polyhedral volume in octahedral sites, and to the degree of coupling of the symmetric and asymmetric stretching vibrational modes of SiO$_4$ groups. Fig. 4a shows the linear trends of the DB1 and DB2 peak positions varying as a function of the atomic masses of the octahedral cations (expressed as $1/\sqrt{M}$, where M is calculated from the averaged cation proportions of the calibration data set in Table 2 weighted according to their atomic masses). Fig. 4b shows the same trend for the full data set. Together, these trends are the scientific basis for developing the olivine calibration.

Doublets from Fe-rich olivine (Fo$_{<50}$) are less well resolved than those of magnesian olivine and the DB2 peak often appears as a shoulder of the DB1 peak. The poorer resolution of the doublet is due to both the broader peak widths and the intrinsically smaller separation of the doublet peaks in fayalite (which results from the less distorted SiO$_4$ tetrahedra and the greater similarity of the M1 and
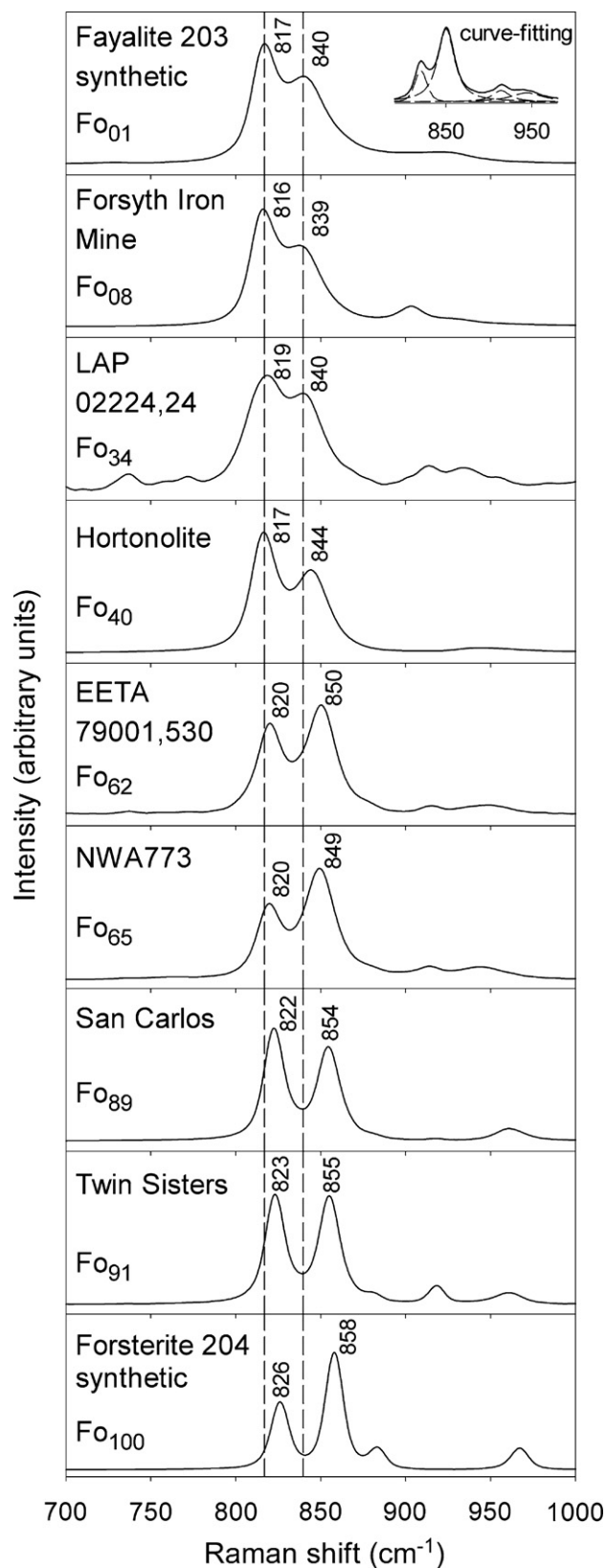

Fig. 3. Raman spectra, 700–1000 cm^{-1} region, from each of the calibration samples plus LAP 02224,24.

M2 octahedra in fayalite). The average peak widths (HHFW—half height full width) of the synthetic Fayalite
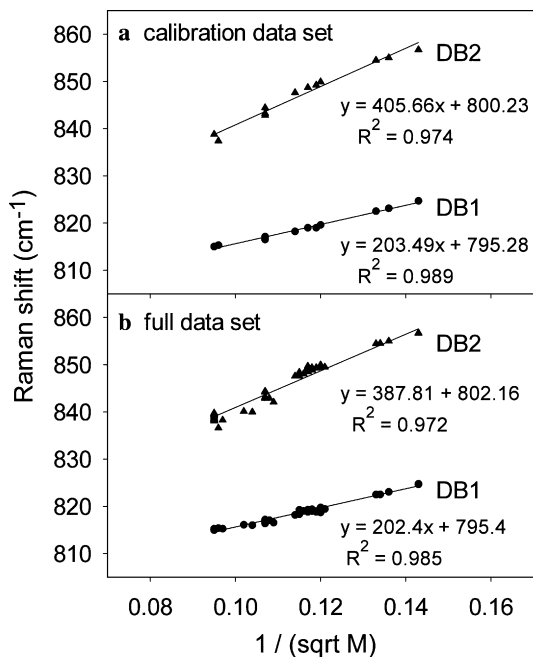
Fig. 4. Correlation of the DB1 and DB2 peak positions versus the reduced mass of Chopelas (1991) $= 1/\sqrt{M}$, where M is the averaged cation mass. The reduced mass was calculated from the cation compositions determined by EMPA for the calibration data set and the full data set. The cation data of the calibration data set is provided in Table 2 and includes the cations Fe, Mg, Mn, Ca, Ni, Cr, and Ti.

203 doublets included in the calibration data set are: $HHFW_{DB1} = 16.5 \pm 0.1 \, cm^{-1}$ and $HHFW_{DB2} = 34.8 \pm 0.5 \, cm^{-1}$; and those of Forsterite 204 are: $HHFW_{DB1} = 12.77 \pm 0.02 \, cm^{-1}$ and $HHFW_{DB2} = 12.74 \pm 0.03 \, cm^{-1}$. Likewise, the average peak separation of the Fa 203 doublet is $\sim 23.8 \pm 0.5 \, cm^{-1}$ and that of Fo 204 is $\sim 31.99 \pm 0.01 \, cm^{-1}$. As such, the uncertainty in the peak positions using spectral curve fitting procedures is larger for Fe-rich olivine (see standard deviations in Table 3). Because the doublet is actually composed of several peaks, it is imperative that an instrument with good spectral resolution (5–7 cm^{-1}) be used to gather remote data so that the DB1 and DB2 peak positions may be adequately estimated.

Studies using polarized Raman measurements indicate that five vibrational modes ($2A_g + 2B_{1g} + B_{2g}$) contribute to the peaks of the doublet (Ishii, 1978; Price et al., 1987; Chopelas, 1991). Considering the peak positions of the modes present and their intensities under different polarization conditions, we conclude that the dominant modes contributing to the olivine doublets observed in unpolarized spectra are the A_g modes. Contributions from the B_{1g} and B_{2g} modes are much smaller but may influence the peak shapes and relative intensities of the doublet and have a minor effect on the peak positions determined by spectral deconvolution.

Davydov coupling of the symmetric stretching (v_1) and asymmetric stretching (v_3) vibrational modes of SiO_4 tetrahedra in the olivine structure has been extensively modeled and tested (Piriou and McMillan, 1983; Lam et al., 1990;

Mohanan et al., 1993). An in-depth review of these hypotheses or follow-up of this discussion is beyond the scope of this study, however, a commonly accepted concept is that both DB1 and DB2 peaks result from coupled v_1 and v_3 modes, and that the degree of coupling is related to the size of the M1 and M2 cations (Piriou and McMillan, 1983). Specifically, the more similar the M1 and M2 octahedra are in size and shape, the less the SiO_4 tetrahedra are distorted and the less the v_1 and v_3 modes are coupled. For example, the M1 and M2 octahedra of γ-Ca_2SiO_4 are even more alike (Quadratic Elongation 1.0062, Angle Variance 27.2, Smyth and Bish, 1988) than that of fayalite because the SiO_4 tetrahedra are less distorted by the large Ca^{2+} cation (radius = 1.08 Å for sixfold coordination, Whittaker and Muntus, 1970), which further reduces the degree of v_1 and v_3 coupling. The pair-potential model of Lam et al. (1990) suggests that inter-tetrahedral O–O and Si–O Coulomb (repulsive) interactions in orthosilicates may also influence v_1 and v_3 mixing and that the influence of these forces is greater on forsterite because the tetrahedra are more skewed by the smaller cation sizes. On the basis of this reasoning and the discussion above on the structural details of forsterite and fayalite, we assume that contributions from the v_1 and v_3 modes vary with the Mg/(Mg + Fe) ratio for both peaks.

A strong, broad peak at 835 cm^{-1} was observed by Chopelas (1991) in the polarized spectrum of synthetic fayalite. This peak was not assigned to a fundamental vibration mode as it is too broad and lacks analogous peaks in other olivine group minerals, but was tentatively related to the Fe^{3+} content in fayalite (0.27–0.86% Fe^{3+}, Finch et al., 1980), while 840 cm^{-1} was assigned as the lower limit (e.g., fayalite) for the DB2 peak (the lowest DB2 peak position in our full data set is 836.6 cm^{-1}). Complications with the DB2 peak assignment and estimating the Mg/(Mg + Fe) ratio of Fe-rich olivine are considered below in the discussion of the calibration.

4. Development and testing of calibrations for Mg–Fe olivine

4.1. "Calibration" vs. "full" data sets

The data used to create and test the calibration were carefully screened from all the paired Raman and EMP analyses on the eight calibration samples (all of the samples listed in Table 1 except LAP and Finch-Robie). The "full" data set, used to evaluate the calibration, includes only those data pairs having EMP totals between 99 and 101 wt%, good stoichiometry, and good resolution of both the DB1 and DB2 Raman peaks. The full data set includes 83 paired data points from the eight calibration samples plus three additional data pairs from a ninth sample, LAP 02224,24. Raman spectra having one peak of the olivine doublet present as only a shoulder of the other peak (usually the DB2 peak as a shoulder of the DB1 peak in the ferroan samples, $Fo_{<50}$) were excluded because the curve-fit data from these spectra appear to underestimate

the DB2 peak positions. The peaks of the doublet are broader in iron-rich olivine and the DB2 peak less well resolved, so a spread of DB2 peak positions was observed in olivine with $Fo_{<50}$, even in the samples whose corresponding EMP data indicated little or no compositional variation (see standard deviations in Table 2).

We averaged the Raman and EMP data from all of the points used in the full data set to create the "calibration" data set (excluding LAP 02224,24). This was done to account for the spread in the observed DB2 peak positions of the ferroan samples and to ensure an even weighting across the range of compositions (culling of the data left the "full" data set with more Mg- than Fe-olivine data points). Seven of the data points in the "calibration" data set represent such averaged Raman and EMP data. Only one spectrum was available from the Twin Sisters dunite and was used by itself in both the full and calibration data sets. The calibration data set *also* includes the Hortonolite data pairs with the highest and lowest DB2 Raman shifts (because this sample had a relatively wide range of DB2 peak positions, although it is unzoned) and the data pairs from the EETA 79001 (xenocrysts zoned only at their rims) with the highest (core) and lowest (rim) Fo values by EMPA. This resulted in a total of 12 averaged EMP and Raman data pairs that were used to create the calibration. The Fo values of these data points are given in Table 2 and their Raman peak positions provided in Table 3.

The calibration data set was used to create and compare potential olivine calibrations from (1) only the DB1 peak positions, (2) only the DB2 peak positions, and (3) the DB1 and DB2 peaks together. The single-peak calibrations represent the best-fit curves to the calibration data set and the best-fit paraboloid for the two-peak calibration. The calibrations are assessed by plotting the Raman-derived Fo contents (calculated from the peak positions of the calibration data set with the respective calibration equation) against the Fo values determined by EMPA and gauging their overall accuracy in terms of which regression line produces the slope and R^2 values closest to one. The modeled Fo contents of the full data set are then plotted against their corresponding EMP-derived Fo values and used to evaluate the quality of the fit of each calibration across the spectrum of olivine compositions. We discuss and compare the single-peak calibrations first, then discuss the two-peak calibration and compare it to the single-peak calibrations. Then we discuss the limitations of the two-peak calibration with respect to mineral zoning and peak resolution. Last, we apply the calibration to a set of spectra from a Raman point-count having less than optimal S/N ratios acquired from two samples of the martian meteorite EETA 79001.

4.2. Calibrations using only one peak of the olivine doublet

Using the twelve data pairs of the calibration data set, we derived a calibration equation to calculate the Mg/(Mg + Fe) ratio using only the DB1 peak position, and a similar equation using only the DB2 peak. Both equations have the form of a parabola (shown in Figs. 5a and b) whose coefficients are listed in Table 4:

$$Fo(DB1) = y_1 + a_1x_1 + b_1x_1^2 \tag{1}$$

$$Fo(DB2) = y_2 + a_2x_2 + b_2x_2^2 \tag{2}$$

where x_i refers to the set of peak positions used (either DB1 or DB2) in the calibration, y_i is the intercept, and a_i and b_i are coefficients. Both the DB1 and DB2 peak positions increase in wavenumber as the Fo content increases. The DB2 single-peak calibration is nearly linear over the observed range of peak positions but the DB1 calibration is curved. Guyot et al. (1986) and Chopelas (1991) both indicate that the component frequencies of the doublet vary linearly according to $1/\sqrt{M}$, where M is the average cation mass (simple harmonic oscillator model). In Fig. 4, the DB1 and DB2 peak positions are plotted against $1/\sqrt{M}$ calculated from the EMP cation data of Table 2, these plots are linear and demonstrate that atomic mass is the major factor causing the DB1 and DB2 peak position shifts. It is possible that the curvature of the DB1 calibration in Fig. 5a results from a change in the degree of coupling of the v_1 and v_3 modes with composition.

Chopelas (1991) suggests that the symmetric stretching frequency v_1 should vary less with composition and Price et al. (1987) use their THB (three-body) potential model to predict the DB1 peak to have more v_1 character than
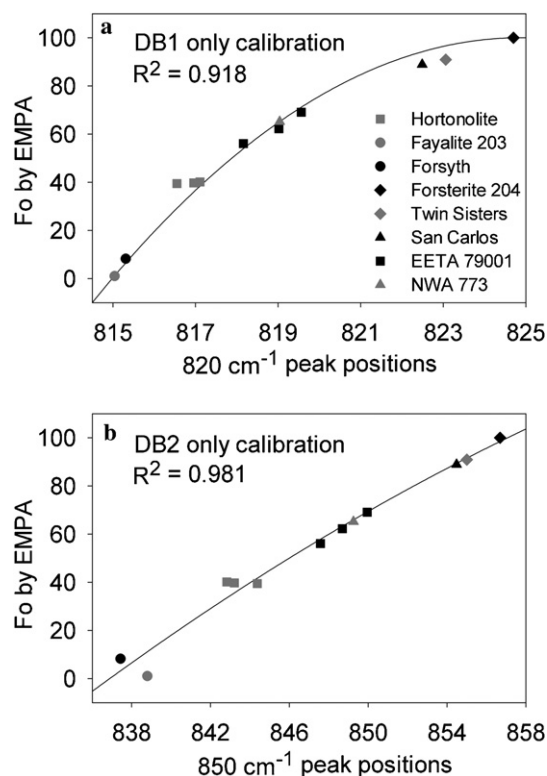

Fig. 5. Single-peak calibration curves created from just the (a) DB1 and (b) DB2 peak positions of the calibration data set with the corresponding Fo values determined by EMPA at the same locations.

Table 4
Intercepts and coefficients for Eqs. (1)–(4)

Equation (i)	y_i	a_i	b_i	c_i	d_i
1	−484679.045145550	1172.7260643126	−0.70922596841326		
2	−38847.125692649	86.908635300809	−0.04838169365694		
3	−206232.988995287	80.190397775029	399.350231139156	−0.0424363912074934	−0.2357973451030880
4	14083.389163575	−31.7969815694767	0.01905011147407		

the DB2 peak in forsterite. These statements agree with our observation that the DB1 peak positions vary less ($\Delta \sim 10\ \text{cm}^{-1}$) across the forsterite–fayalite compositional range than the DB2 peak positions ($\Delta \sim 20\ \text{cm}^{-1}$).

4.3. Comparison of the single-peak calibrations

To evaluate and compare the accuracy and precision of the Fo values calculated from the two single-peak calibration equations (Eqs. (1) and (2)), we plotted the Fo values determined by EMPA against those calculated from the DB1 and DB2 Raman peak positions with their respective equations. First, the calibration data set is used to gauge the accuracy of the single-peak calibrations (Figs. 6a and

b), then the full data set is used to gauge precision across the range of compositions (Figs. 6c and d).

The DB2 peak has a wider range of observed peak positions ($\sim 20\ \text{cm}^{-1}$) from fayalite to forsterite than the DB1 peak ($\sim 10\ \text{cm}^{-1}$) and was expected to give a tighter correlation to the Fo values. However, scatter in the observed DB2 peak positions (Fig. 6b) below Fo_{50} limits the accuracy of this single-peak calibration for Fe-rich compositions. As a result, the Fo values based on the DB1 data in Fig. 6a are slightly less scattered, $R^2 = 0.988$, than those based on DB2 data in Fig. 6b, $R^2 = 0.981$. The slopes of the regression lines are 1.07 and 0.98, respectively. Only the Hortonolite data point representing the highest DB2 peak position falls outside the 99% confidence intervals in Fig. 6a, with a
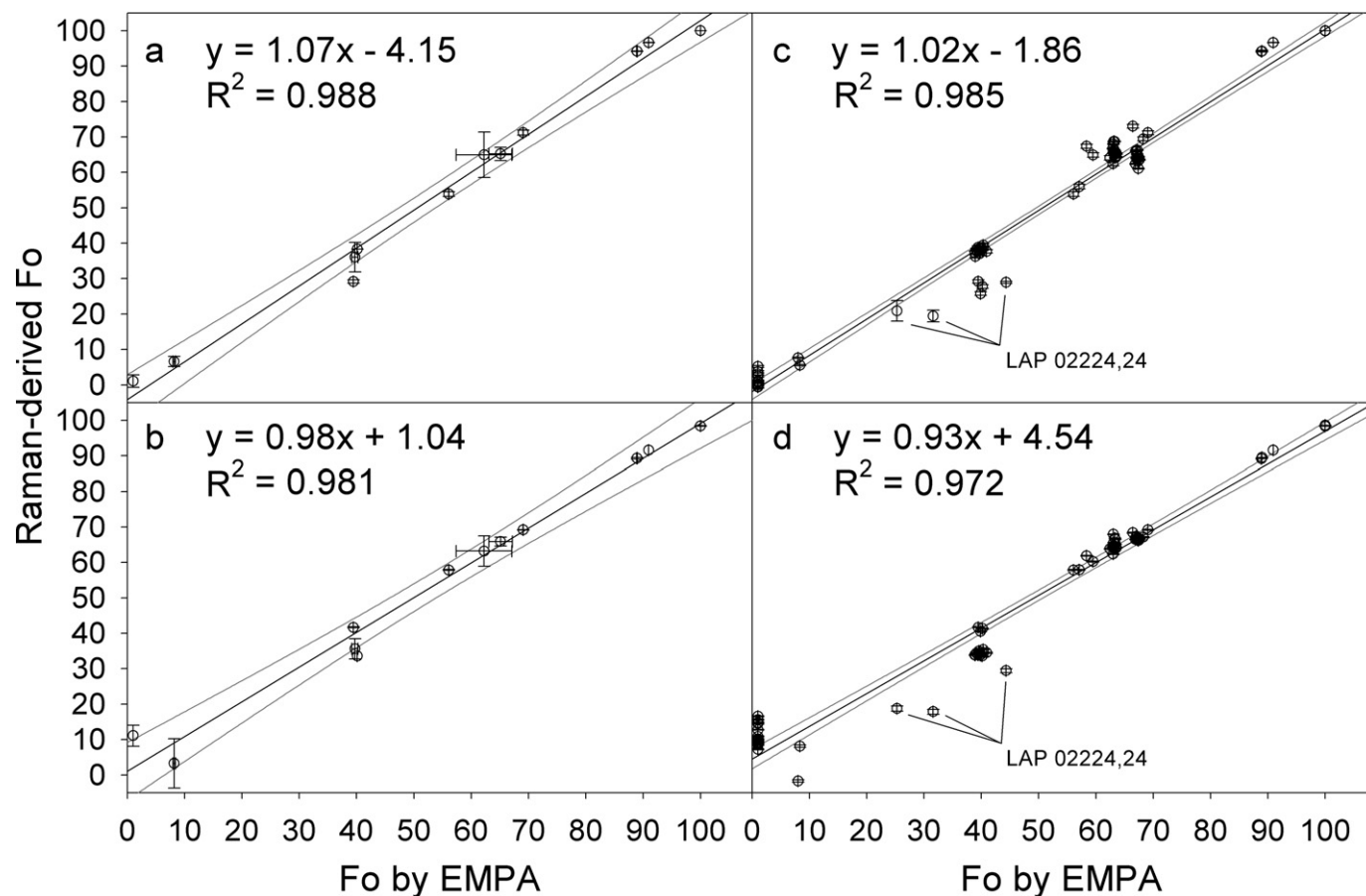

Fig. 6. Forsterite values derived from the DB1 (a and c) and DB2 (b and d) single-peak calibrations plotted against the Fo data determined by EMPA for the calibration (a and b) and full (c and d) data sets. Solid black lines: linear regressions, solid gray lines: 99% confidence intervals. The Raman derived Fo values of the three data points from the strongly zoned olivine of LAP 02224,24 in the full data set are underestimated by both single-peak calibrations and are labeled in (c and d).

discrepancy of ~10.3 Fo units between that measured by EMPA and that predicted by the DB1 single-peak calibration. Otherwise, all of the DB1-predicted values are within Fo ±7. Two data points fall outside the 99% confidence intervals in Fig. 6b (DB2 single-peak calibration): Fa 203 and the Hortonolite data point representing the lowest DB2 peak position. The Fo contents predicted by the DB2 single-peak calibration for these points differ by 10.1 and 6.6 Fo units, respectively, from that measured by EMPA. The 99% confidence intervals are tightest for intermediate compositions for both calibrations and are slightly narrower for the DB1 calibration (Fig. 6a) than for the DB2 calibration (Fig. 6b).

The error bars shown in Figs. 6a and b for the EMP data are the standard deviations of the Fo values of the analyses used in the averaged data set (see Table 2). The error bars for the Raman-derived Fo values were determined by error propagation from the standard deviation of the curve-fit Raman peak positions for all of the samples from which multiple spectra were available. If only a single spectrum was available we used replicate curve-fitting analyses to provide error estimates for the peak positions. Such was the case for the Twin Sisters Dunite, the Hortonolite spectra with the maximum and minimum DB2 peak positions, and the EETA data points with the maximum and minimum Fo values. These error estimates are smaller than those determined from multiple spectra (see Table 3). The error bars are less than or equal to the size of the symbols used for most data points. The average EETA 79001 data point has error bars larger than its symbol in both Figs. 6a and b, which reflects zoning at the rims of these xenocrysts. The average Hortonolite data point has larger error bars for its Raman-derived Fo values than either of the upper or lower DB2 points because the standard deviation of the average DB2 peak position is larger than that determined for the single peaks. Fayalite 203 and Forsyth have larger error bars for their DB2-predicted Fo values than their DB1-predicted Fo values because the standard deviations of the DB2 peak positions are larger.

When the Raman-derived Fo values of the full data set are plotted against the Fo values from EMP analyses, we find that the DB1 calibration (Fig. 6c, slope = 0.944, $R^2 = 0.985$) is generally better for fayalitic compositions, whereas the DB2 calibration (Fig. 6d, slope = 0.925, $R^2 = 0.972$) is better for intermediate and forsteritic compositions. There is considerably more scatter in the Fo_{50-100} range when using the DB1 calibration where most common olivine compositions occur, but the DB2 peak calibration has even larger deviations for fayalitic compositions (discrepancies of up to 15.5 Fo units between the EMP and Raman-derived Fo values), which are important for understanding late-stage cooling in igneous rocks. The predicted Fo values of some Hortonolite points are underestimated and fall outside the 99% confidence intervals in both Figs. 6c and d. Three Hortonolite points are underestimated by 10–14 Fo units in Fig. 6c (points having DB1 peak positions <816.7 cm^{-1}) but the rest are predicted val-

ues to within Fo ± 3.1 (data with DB1 peak positions of 817.0 and 817.1 cm^{-1}). The same three Hortonolite points are slightly overestimated (~2 Fo units) by the DB2 single-peak calibration. The other points (having DB2 peak positions between 842.8 and 843.1 cm^{-1}) fall outside the 99% confidence interval in Fig. 6d and are underestimated but are all within Fo ± 7 of their EMP values.

These discrepancies occur because a range of DB2 peak positions are observed in the spectra of Fe-rich samples ($Fo_{<50}$), even those whose EMP data indicate little, if any, compositional variation (see standard deviations in Table 2). The two clusters of data points indicate difficulties with the curve-fit peak positions of the Hortonolite spectra. The DB1 single-peak calibration is more accurate for predicting the compositions of fayalite and appears to be more accurate for Fo_{10-50} compositions, as well, since it predicts the LAP 02224,24 compositions better (Figs. 6c and d). The DB1 peak is the taller of the two peaks in all of these spectra so its curve-fit peak positions are probably the more accurate. Because neither single-peak calibration is useful for all olivine compositions and because curve-fitting issues may arise in ferroan olivine, a calibration using both peak positions of the olivine doublet is desirable to minimize errors across the Mg/(Mg + Fe) spectrum.

It is possible that the DB2 peak positions of the ferroan samples include contributions from additional vibrational modes. Chopelas (1991) observed two broad features in the A_g symmetry (one occurring near 835 cm^{-1}) of a synthetic fayalite that are not fundamental modes; she attributed these to the presence of Fe^{3+} in the sample. Interference of such a feature with the DB2 peak (whose lower limit is estimated to be ~840 cm^{-1}, Chopelas, 1991) could hinder curve-fitting results and influence the inferred range of DB2 peak positions in fayalite. We discuss the potential presence and influence of Fe^{3+} in our data set after presenting the two-peak calibration.

The error bars used for the individual EMP data points in Figs. 6c and d were determined by averaging the standard deviations from three EMP analyses on each of the synthetic fayalite and forsterite and assuming this to be representative of all EMP analyses. The error bars used for the Raman-derived Fo values are based on ten replicate curve-fitting analyses of a single spectrum from each sample and assuming these to be representative of all spectra from the same sample. Again, the error bars are comparable to the size of the symbol used.

4.4. Calibration using both peaks of the olivine doublet

The twelve data pairs (Tables 2 and 3) were used to derive a calibration equation that depends on both the DB1 and DB2 peak positions. This calibration equation represents a best-fit paraboloid to the twelve points shown in the three-dimensional plot, Fig. 7a. The paraboloid is shown in Fig. 7b and has the form:

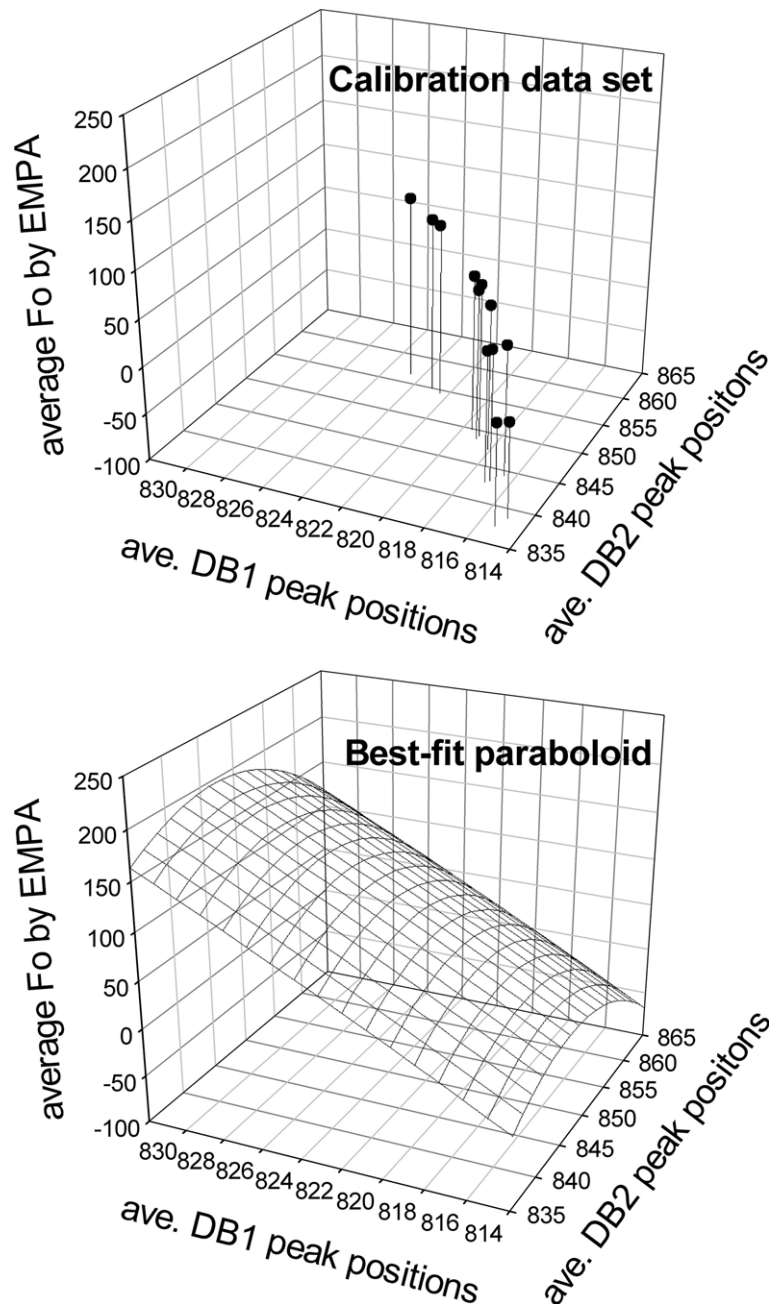$$Fo(DB1 \ \& \ DB2) = y_3 + a_3x_1 + b_3x_2 + c_3x_1^2 + d_3x_2^2 \qquad (3)$$

Fig. 7. Three-dimensional plots of (a) the calibration data set (DB1, DB2 and Fo values) determined from co-registered Raman spectra and EMPA data, where Fo = Mg/(Mg + Fe + Mn), molar ratio. The two-peak calibration, shown in Fig. 8, was created by projecting solutions of (b) the best-fit paraboloid (Eq. (3)) onto the plane of the DB1 and DB2 peak positions.

where x_1 is the DB1 peak position, x_2 is the DB2 peak position, y_3 is the intercept, and a_3, b_3, c_3, and d_3 are the coefficients listed in Table 4. A two-dimensional projection, shown in Fig. 8a, was generated as a simplification of the three-dimensional plot, made by projecting the data points in Fig. 7a onto the plane of DB1 vs. DB2 peak positions. The central solid curved line of the two-peak calibration diagram is the best-fit parabola to these data points and is represented by an equation of the form:

$$\text{DB1 peak position} = x_1 = y_4 + a_4 x_2 + b_4 x_2^2 \qquad (4)$$

where x_2 is the DB2 peak position, y_4 is the intercept, and a_4 and b_4 are the coefficients given in Table 4. The Fo value "contours" (dashed lines) were made by projecting solutions to the paraboloid (Eq. (3)) onto the plane of DB1 and DB2 peak positions. The points where these divisions intersect the best-fit curve were located using Eqs. (3) and (4) in combination to find the points on the curve where Fo = 10, 20, etc.
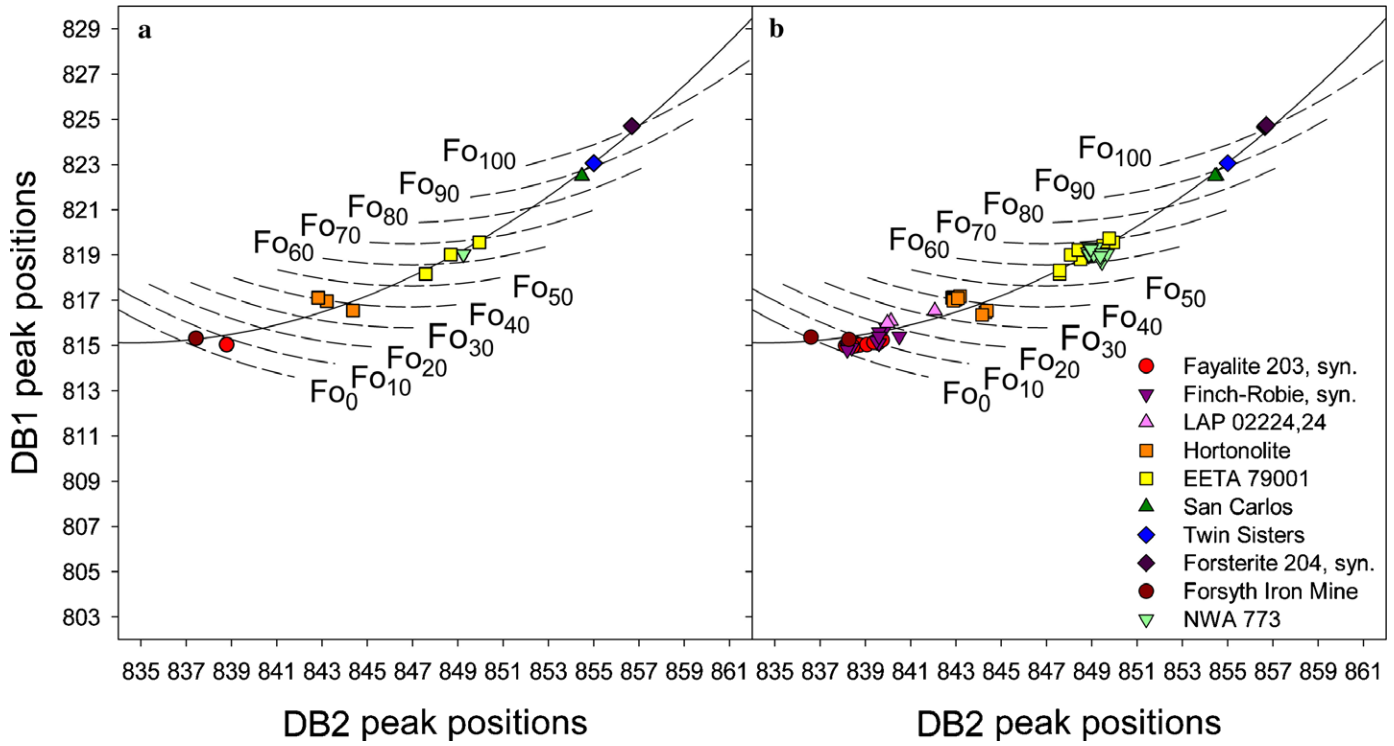
Fig. 8. (a) Two-peak calibration made by projecting the peak positions of the calibration data set onto the plane of DB1 and DB2 peak positions, and finding the best-fit parabola. (b) Two-peak calibration with full data set plus LAP 02224,24 and the Finch-Robie sample. Note the spread in DB2 peak positions for all samples with $Fo_{<50}$, see text for discussion.
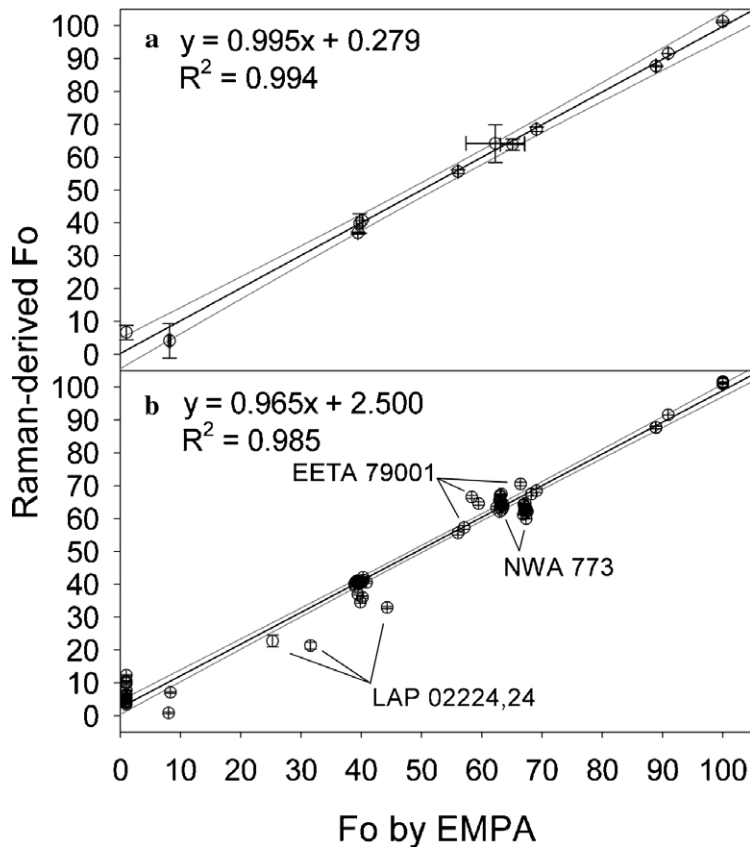

Fig. 9. (a) Forsterite values derived from the two-peak calibration vs. those determined by EMPA for the calibration data set and (b) the full data set (including LAP 02224,24). Solid black lines: linear regressions, solid gray lines: 99% confidence intervals. Data points from EETA 79001, NWA 773, and LAP 02224,24 are labeled for reference in (b), see text for discussion.

4.5. Evaluation of the two-peak calibration

The Raman peak positions of the calibration data set are plotted on the two-peak calibration in Fig. 8a and are generally observed to fall along the central, solid curve except the three Hortonolite points that appear to straddle it. The full data set is shown in Fig. 8b (including LAP 02224,24) where a little more scatter is apparent. Scatter in the EETA data points (Fo_{55-70}) can be attributed to zoning at the rims of the olivine xenocrysts, but 1.5–2 cm^{-1} of scatter is apparent in the DB2 peak positions of the chemically homogeneous ferroan olivine (both synthetic fayalites, Forsyth, and Hortonolite). The Fayalite 203 data distribution is smooth but the Hortonolite data fall into two clusters on either side of the central curve and one of the two Forsyth Iron Mine (Fo_{10}) data points has a DB2 peak position of 836.6 cm^{-1}—lower than all of the synthetic fayalite points, whose DB2 peaks range down to 838.1 cm^{-1}.

The DB1 and DB2 peak positions of the calibration data set were used with Eq. (3) to find the Fo values predicted by the two-peak calibration and plotted against the Fo values of the corresponding EMP data. The regression shown in Fig. 9a approximates a 1:1 correlation better than either single-peak calibration (slope = 0.995 and $R^2 = 0.994$). The data are less scattered and have narrower 99% confidence intervals, implying a tighter correlation with the calibration data set. Likewise, the Raman-derived Fo values of the full data set are plotted against their corresponding EMP Fo values in Fig. 9b; the R^2 (=0.985) is closer to 1 than either of its single-peak counterparts and the slope slightly less than 1. There is more scatter in the Fo_{50-100} range of the full data set in Fig. 9b than that of the DB2 single-peak calibration of Fig. 6d (Eq. (2)), but less than that using the DB1 single-peak calibration in Fig. 6c (Eq. (1)). Deviations still occur at fayalitic compositions in Fig. 9b but are comparable to those of the DB1 single-peak calibration and less than those of the DB2 single-peak calibration. Most of the predicted values are within ±10 Fo units of their EMP values; only one Fa 203 and two LAP 02224,24 data points (discussed later), fall outside this range, illustrating that it is possible to use the two-peak calibration to estimate the compositions of unoriented olivine, including fayalite, from their Raman peak positions (even spectra collected using an unpolarized laser) within Fo ± 10.

As in Figs. 6a and b, the error bars used for the EMP data in Fig. 9a are the standard deviations of the electron microprobe analyses used in the calibration data set. In Fig. 9b, the error bars of the EMP data are the averaged standard deviations of three analyses on each of the synthetic fayalite and forsterite. Likewise, the error bars on the Raman-derived Fo values in Figs. 10a and b come from the standard deviations of the peak positions wherever multiple spectra are used and from replicate curve-fitting analyses for single spectra.
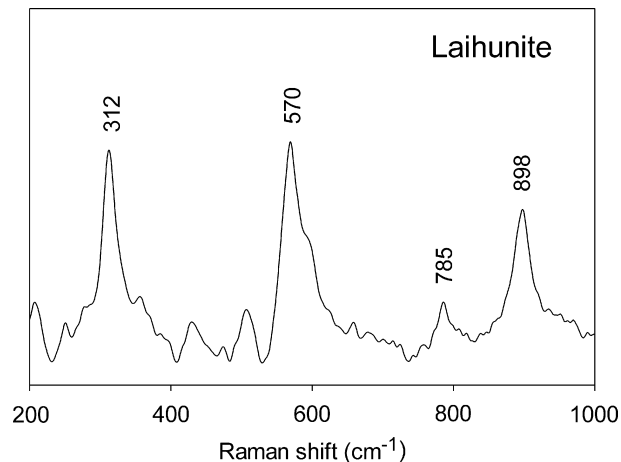

Fig. 10. Spectrum of laihunite, a monoclinic mineral with a composition similar to fayalite but containing significant Fe^{3+}.

4.6. Variability of DB2 peak positions and spectral resolution requirements for planetary surface investigations of ferroan olivine

A range of DB2 peak positions is apparent for the ferroan samples in Fig. 8b but these data do not represent the full range of DB2 peak positions observed in *all* of the data we collected. In the process of reviewing the data, spectra were discovered for which the curve-fitting routine appeared to underestimate the DB2 peak positions (data excluded from both the calibration and full data sets). This occurred with spectra from fayalitic samples whose DB2 peak height was only half that of the DB1 peak and hence appears as only a shoulder of that peak. The presence of the DB2 peak as only a shoulder of the DB1 peak formed the criteria for the removal of spectra from the data sets (instead of selecting an arbitrary cut-off peak position) and describes the majority of the data collected from the Forsyth and Finch-Robie fayalite (27 of 30 and 19 of 31 spectra, respectively) but only 5 of 20 spectra from Fayalite 203, despite analyzing the samples at multiple orientations. A range of DB2 peak positions is also observed in the Hortonolite spectra but all of its DB2 peak positions are >840 cm^{-1} and sufficiently resolved, so that none were excluded from the full data set.

We attribute the range in DB2 peak positions to contributions from the 835 cm^{-1} feature observed by Chopelas (1991). The DB2 peak positions used to create the calibration range down to 836.6 cm^{-1}, below the estimated lower DB2 limit of Chopelas (1991), <840 cm^{-1}, but the excluded data have DB2 peak positions that range almost 1.5 cm^{-1} lower, down to 835.2 cm^{-1}. The spectral resolution of our laboratory system (HoloLab 5000®) is 6.2 cm^{-1} and that of the Mars Microbeam Raman Spectrometer (MMRS) brassboard is 8–9 cm^{-1} (Wang et al., 2003b). Considering that the calibration spectra were collected in the laboratory, have good signal-to noise ratios (S/N) and that data collected from Raman point counts on rough

rock surfaces will typically have lower S/N ratios, good spectral resolution (5–7 cm^{-1}) will be key to ensuring reliable Fo estimates for remotely analyzed Fe-rich olivine, especially fayalite.

As mentioned previously, the 835 cm^{-1} feature has been attributed to the presence of Fe^{3+} (Chopelas, 1991). The Finch-Robie sample contains <1% Fe^{3+} and is the fayalite for which the 835 cm^{-1} feature was first reported (Finch et al., 1980; Chopelas, 1991). Imperfections noted in the Finch-Robie olivine include evidence for cellular growth, prominent voids, and magnetite and Fe-Si inclusions (Finch et al., 1980). Magnetite and OH peaks appear in both of the Forsyth spectra included in the full data set. Two of the sixteen Hortonolite spectra also have small magnetite peaks, and five contain weak OH peaks. Both the magnetite and OH peaks imply oxidation of the Forsyth and Hortonolite samples so the potential influence of Fe^{3+} in these samples needs to be considered as well. However, none of the spectra acquired from the synthetic Finch-Robie sample contain magnetite or OH peaks, nor do the spectra from the synthetic Fa 203, which should not contain any Fe^{3+} and does not contain any magnetite inclusions. Nevertheless, a range in DB2 peak positions was observed in all four samples. We, therefore, question whether this feature is attributable to Fe^{3+} but explore substitution by Fe^{3+} as well as other potential sources (Mn substitution, presence of OH) for the range of DB2 peak positions.

The radius of $^{(VI)}$Fe^{3+} (0.73 Å, high spin) is smaller than that of $^{(VI)}$Fe^{2+} (0.86 Å, high spin, Whittaker and Muntus, 1970) so very little Fe^{3+} should occur in the crystal structure of primary olivine. Laihunite is a mineral with the composition of fayalite that contains significant Fe^{3+}; it has a monoclinic structure and a very different Raman spectrum (Fig. 10). In comparison to the olivine structure, Fe^{3+} in laihunite is partitioned into M2 sites and Fe^{2+} into M1 sites with vacancies occurring in alternate rows parallel to (001) for charge balancing (Dyar et al., 1998). Solid solutions between laihunite and fayalite are loosely referred to as "ferrifayalite" while the terms "ferriolivine" and "oxidized olivine" are used to describe olivine structures that contain inter-layered phases such as magnesioferrite and magnetite (Khisina et al., 1995), hematite and amorphous silica (Ishii et al., 1997), or humite-like layers (Kitamura et al., 1984). The difference in the radii of $^{(VI)}$Fe^{2+} and $^{(VI)}$Fe^{3+} is 0.13 Å, twice that of $^{(VI)}$Fe^{2+} and $^{(VI)}$Mg^{2+}, 0.06 Å. The resulting distortion of the M1 and M2 octahedra, would hypothetically produce an increased coupling of modes in Fe^{3+} bearing olivine, and have a greater effect on the asymmetric stretching (v_3) vibrational modes and the DB2 peak positions. However, the EMP totals from the Forsyth and Hortonolite olivine are good and the stoichiometry indicates no need for including Fe^{3+} in the calculation of their cation proportions. Therefore, we assume that only minor Fe^{3+} is present in these olivine, despite the magnetite and OH peaks.

The Forsyth sample contains almost 1 wt% MnO and the Hortonolite about half that. The ionic radius of $^{(VI)}$Mn^{2+} = 0.91 Å (high spin) is slightly larger than that of $^{(VI)}$Fe^{2+} (Whittaker and Muntus, 1970) but their atomic weights differ by only 1.1 amu and their charges and ionic potentials are also similar. Burns and Huggins (1972) demonstrated that the four infrared bands that vary with composition across the forsterite–fayalite series vary less across the fayalite–tephroite series (having monotonic downshifts of 1, 5, 12, and 11 cm^{-1}) and Cooney and Sharma (1990, Table 3, band 2) showed that the variation in Raman peak positions across the breadth of forsterite–tephroite glass compositions is equivalent to that observed for glasses of forsteritic to fayalitic compositions. We therefore expect that Mn substitution of less than a few wt% will have little influence on the Raman peak positions, perhaps a few tenths of a wavenumber. Note: Mn^{2+} substitutes readily for Fe^{2+} and was included in the calculation of the Fo values from the EMP data; the Fo values of all samples changed by less than 1.5% relative to the Fo values determined without the Mn, such that all values in Table 2 changed by <0.005. The largest changes are observed in the Forsyth and Hortonolite samples, 1.3% and 0.8%, respectively. Substitution by greater proportions of Mn^{2+} could potentially cause anomalously low peak positions but Ca^{2+} substitution (Ca also prefers M2 sites) would be expected to have a larger effect owing to its smaller mass and larger cation size (1.08 Å, Whittaker and Muntus, 1970). The Finch-Robie sample contains <10 ppm Mn (Finch et al., 1980) and our EMP data indicate that the synthetic Fa 203 contains <0.1 wt% MnO, so Mn substitution also appears to be an unsatisfactory explanation for the 835 cm^{-1} feature.

The Forsyth spectra contain solitary OH peaks occurring between 3620 and 3630 cm^{-1}; the Hortonolite spectra have more variable peak patterns and peak positions but the OH peaks generally occur in the same region as those of the Forsyth sample: 3600–3700 cm^{-1}. None of the spectra from the Fa 203 and Finch-Robie samples contain OH peaks, nor has either of these two synthetic samples been reported to contain OH, so we similarly disregard the presence of OH as the source of the 835 cm^{-1} feature.

The range of DB2 peak positions (1.5 cm^{-1}) shown for Fa 203 in Fig. 8b is interpreted to result from imprecision in the curve-fitting results of the overlapping peaks of the doublet, with possible contributions from a feature at 835 cm^{-1}. The observed range of DB2 peak positions for the Finch-Robie sample is slightly wider (2.3 cm^{-1}) than that of the Fa 203 while the Hortonolite and Forsyth ranges are comparable (1.6 and 1.7 cm^{-1}, respectively). We presume that removal of the data points having underestimated DB2 peak positions remediated some of the contributions of the 835 cm^{-1} feature from the calibration data, but regard the apparent influence of this feature in all four of the ferroan samples reviewed here as an indication of its commonality in the spectra of ferroan olivine. The collective properties of the synthetic Fa 203, Forsyth,

Hortonolite, and Finch-Robie samples contraindicate the presence of Fe^{3+}, Mn, and OH as the potential source of this feature but we did not identify any other common feature among the four Fe-rich samples to suggest as an alternate explanation. On the basis of this discussion, we propose that use of the two-peak calibration be restricted to curve-fit data whose DB2 peak positions are >837 cm^{-1}.

4.7. Tolerance of the olivine calibration to mineral zoning

Olivine grains in the lunar meteorite LAP 02224,24 are strongly zoned in chemical composition. EMPA indicates zoning from Fo_{26} to Fo_{46} within 75 μm in LAP 02224,24, which equates to zoning of ∼2 Fo units within the diameter of the Raman excitation laser beam, when it is in focus. Two of the points from LAP 02224,24 deviate from the regression line in Fig. 9b. Deviation is partly attributed to the different compositions "seen" by the two techniques in samples zoned on a fine scale (relative to the scale of the area being analyzed). Zoning on a fine scale, however, also produces spectra with broader and less well-resolved peaks due to the overlapping of mode frequencies and introduces short-range translational disorder in the framework of the olivine structure. Translational disorder produces variable peak shifts and broader peaks, which influence the accuracy of the Raman-derived Fo values. The calibration predicts the composition of one LAP data point to within 3 Fo units of the EMP-derived value (an underestimate) but was less accurate with the other two points, whose Raman-derived Fo values are ∼10–11 Fo units less than those determined by EMPA.

Olivine xenocrysts in martian meteorite EETA 79001,530 are compositionally zoned at their rims (from $Fo_{60–80}$) and have broader DB1 and DB2 Raman peaks that are also less well-resolved. The EETA 79001,530 data in Fig. 9b scatter more than the NWA 773 olivine, which are similar in composition. Zoning occurs over a wider distance in EETA 79001, ∼400 μm, equating to ∼0.4 Fo units in the diameter of the Raman excitation laser beam, in focus. All of the Fo values calculated from the two-peak calibration for EETA 79001,530 data are within 10 Fo units of those measured by EMPA. These two compositionally zoned samples (LAP 02224,24 and EETA 79001,530) help constrain the tolerance of the two-peak calibration to ∼0.5–1.0 Fo units of zoning within the diameter of the laser beam (∼6 μm) before the discrepancy between the Raman and EMP-derived Fo values deviate more than 10 Fo units.

5. Raman point counting of EETA 79001 rock chips—Use of the two-peak olivine calibration with low signal-to-noise data

Of the 560 spectra collected on rock chip EETA 79001,476, 114 contain peaks belonging to olivine. Likewise, 72 of the 560 spectra collected from the four EETA 79001,482 rock chips contain olivine doublets. Because the data were collected by Raman point counting, i.e.,

on rough rock surfaces, typically off-focus with multiple mineral phases present in most spectra, the sampled volumes are larger and the observed S/N ratios vary from strong to poor (see Fig. 11). Although $>99\%$ of the spectra contain peaks adequate for mineral identification (Wang et al., 2004b), many olivine doublets are less well resolved compared to the spectra used in the previous sections. The low S/N ratios and lower resolution introduces uncertainties in determining the spectral peak positions and influences the accuracy of the Raman-derived Fo estimates.

Wang et al. (2004b) reviewed all of the Raman point count data from these samples, and demonstrated how to distinguish related lithologies and extract petrographic data from mineral calibrations such as this. Our purpose in revisiting the olivine spectra of this data set is to gauge the amount of signal processing and the minimum S/N ratio needed to produce reliable Fo estimates. We
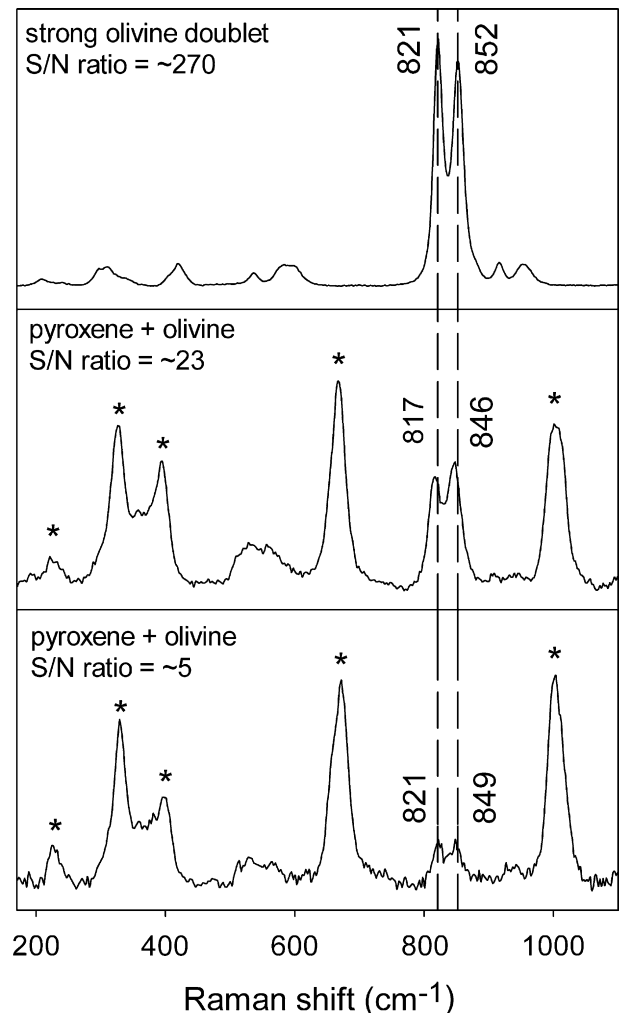

Fig. 11. The signal-to-noise (S/N) ratios of spectra acquired during a point count can range from strong to poor. Shown here are three spectra from rock chips of EETA 79001,482 demonstrating the range of S/N ratios of the olivine doublets used in the discussion. Asterisks indicate peaks belonging to pyroxene.

also examine the low S/N doublets that scatter away from the calibration curve and suggest how to extract information from these spectra if the overall quality of the Raman point count is low or the data otherwise scant.

All of the olivine doublet data from the two EETA 79001 rock chips were plotted on the two-peak calibration in Figs. 12a and b. The peak positions used in Fig. 12a come from visually locating the symmetric center of the DB1 and DB2 peaks after baseline subtraction. Fig. 12b is the same plot using curve-fit peak positions. In both of the plots, the majority of the data fall along the solid central curve in the range of Fo_{50-85}, which agrees quite well with the published range, Fo_{55-81} (Steele and Smith, 1982; McSween and Jarosewich, 1983).

Histograms of the Fo values calculated from the data shown in Figs. 12a and b are shown in Figs. 13a and b and are generally consistent with Wang et al. (2004b), although smaller bins are used here. Such histograms may be used to make inferences about a sample's cooling history (Wang et al., 1999, 2004b). For example, the single broad peak of Fo values in rock chip EETA 79001,482 (Fig. 13) indicates a simple cooling history, typical of basalt, as does the histogram of Raman-derived pyroxene ratios (Mg/ (Mg + Fe + Ca), see Fig. 7b of Wang et al., 2004b). The histogram made from the olivine in EETA 79001,476 has a bimodal distribution that indicates the presence of xenocrystic olivine. The mode at higher Fo values ($\sim Fo_{70-80}$) corresponds to the xenocrystic olivine (higher than the Mg/ (Mg + Fe + Ca) of any groundmass pyroxene) and the olivine mode at median Fo values (Fo_{50-60}) corresponds to olivine equilibrated with the pyroxene in the surrounding groundmass as discussed in Wang et al. (2004b).
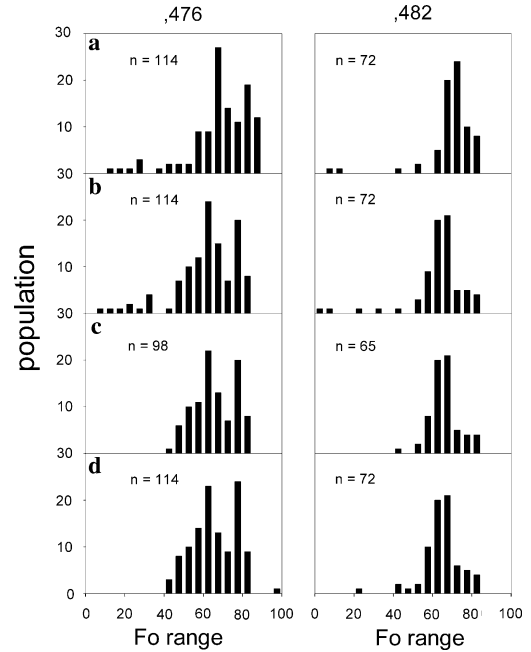

Fig. 13. Histograms produced from the Fo estimates of the data set (a) after baseline subtraction only, (b) after curve-fitting, (c) with the scattered data points removed, and (d) substituting the Fo estimates calculated from the DB2 single-peak calibrations for the scattered data points. The histograms for EETA 79001,476 show a bimodal distribution of olivine compositions but those of 79001,482 indicate a unimodal distribution, signaling locally different cooling histories.

Figs. 12a and b appear substantially the same, with the majority of the data falling on the solid, central curve and the rest scattering below it. The curve-fit data that fall along the median curve in Fig. 12b are slightly less scattered so curve fitting appears to have modestly
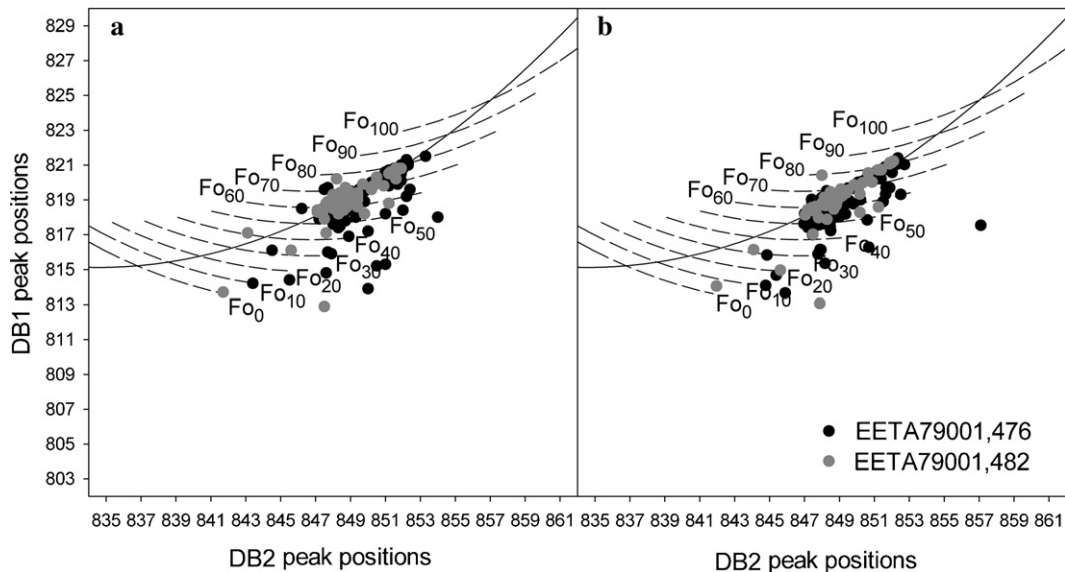

Fig. 12. EETA 79001 rock chip data on the two-peak calibration using peak positions (a) from baseline subtracted spectra and (b) after curve-fitting of the olivine doublets. Curve-fitting reduces the scatter in spectra with moderate to strong signal-to-noise ratios (those falling along or near the central curve) but does not improve Fo estimates from doublets with very low signal-to-noise ratios (i.e., those that scatter >2 wavenumbers away from the curve).

improved the data. This improvement is more readily apparent in the histograms of Figs. 13b, which have sharper peaks, and reveal that the Raman-derived Fo values of many data points decreased enough to shift the peaks of the histograms down one bin. Curve-fitting did not significantly decrease the scatter (neither the number of scattered points or the extent of scattering) in the data points that initially strayed away from the median curve, however.

All of the data points that fall away from the median curve in Figs. 12a and b come from olivine doublets with low S/N ratios. Scatter is greater than that observed in the EETA 79001,530 calibration data and may be attributed to a combination of factors including zoning, the reduced S/N, and poorer peak resolution of the rock chip data. All of the scattered doublets have S/N ratios <25 for both peaks, whereas the average S/N ratio for all of the doublets from rock chip,476 is 50 and 85 for,482 (not all low S/N data points scatter, however). The lower S/N and peak resolution produce larger uncertainties in the DB1 and DB2 peak positions and explain why curve fitting does not significantly reduce the scatter in Fig. 12b (curve-fitting increases the scatter of two data points, see discussion below). From this, we interpret that curve-fitting can improve the accuracy of the Raman-derived Fo values from olivine doublets with below average S/N ratios (e.g., between 25 and 50 for this data set) but not those with very weak doublets (<25).

One consequence of significant scatter (>1.5 cm^{-1} away from the central curve) is that the Raman-derived Fo estimates of the scattered data are higher or lower than those falling on the curve (depending on whether they scatter above or below the central curve), and likely in error. This is a result of how the paraboloid (Eq. (3)) projects onto the two-peak calibration, producing the curved forsterite divisions shown in Figs. 8 and 12. We recommend using the single-peak calibrations to reevaluate the Fo content of these data points. The following discussion of the scattered data points from EETA 79001 illustrates our reasoning for this.

Comparing the distribution of the data points in Figs. 12a and b to the histograms in Figs. 13a and b, it is apparent that the tails of the histograms at moderate to ferroan compositions do not correspond to data points falling on the central curve at these values. Although Wang et al. (2004b) cite instances of late-stage fayalite-pyroxene-silica symplectite in thin section EETA 79001,357 and a few olivine of Fo$_{30–40}$ in thin section EETA 79001,442 by EMPA, the ferroan olivine proportions indicated by the histograms in Figs. 13a and b are due to the scattered, low S/N data points and are overestimated. Contextual information will aid in the assessment of scattered data points in remotely acquired data sets. For example, the coexistence of ferroan olivine with low-Mg pyroxene and other late-stage mineral phases found in the groundmass of the meteorite is consistent with the interpretation of the mineral assemblage as of

a late-stage basaltic mesostasis (see Fig. 9 of Wang et al., 2004b).

The S/N ratio of remotely analyzed samples will vary greatly from one rock to another, depending on the surface roughness and sample geometry. When many good olivine spectra are available, the data points that scatter away from the curve (or those with S/N ratios <25) may simply be removed before analyzing the data further. If the olivine data are poor or scarce, the scattered points will be more valuable; in which case, one can use the single-peak calibrations to estimate the Fo contents of the scattered points. Although both of the peak positions of a scattered data point will probably be affected by the low S/N and poor peak resolution, we can use the compositions of the good data to indicate which single-peak calibration should be used to re-evaluate the Fo contents of the scattered data.

Nearly all of the scattered EETA data points fall below the median curve so the Raman-derived Fo values from Eq. (3) are underestimates. Although it may not be strictly true, we assume that the scattered data points should fall within the same range of compositions as the good data points, Fo$_{50–85}$, compositions that the DB2 single-peak calibration is better at predicting.

A comparison of the Fo values calculated for the scattered data points in Fig. 12b from the single-peak (Eq. (1)—DB1 and Eq. (2)—DB2) and two-peak calibrations (Eq. (3)) is presented in Table 5. The Fo values calculated

Table 5
Comparison of Fo values predicted by the single and two peak calibrations for the data points that scatter in Fig. 10b

	DB1 peak after cf	DB2 peak after cf[a]	Predicted Fo DB1 only	Predicted Fo DB2 only	Predicted Fo two-peak
EETA,476					
oct2949	814.1	844.8	−13.4	43.8	10.3
oct2952	817.8	850.6	50.3	72.2	49.0
oct3075	818.9	851.5	63.3	76.4	58.5
oct3126	814.7	845.4	−1.7	46.9	17.3
oct3138	816.1	847.9	24.6	59.6	33.5
oct3238	819.7	851.7	71.8	77.1	66.7
oct3240	819.3	851.6	67.9	77.0	62.7
oct3263	819.7	851.9	71.6	78.0	66.1
oct3319	815.8	844.9	19.5	44.2	29.6
oct3322	815.9	847.8	20.5	58.8	30.9
oct3433	816.1	847.9	24.8	59.4	33.6
oct3482	819.3	852.5	67.8	80.8	60.4
oct3503	817.5	857.1	46.1	100.1	24.1
oct3505	815.3	848.2	11.0	60.8	24.8
oct3527	816.3	850.7	27.1	72.6	31.8
oct3558	813.7	845.9	−22.5	49.5	6.3
EETA,482					
nov0213	818.3	850.2	56.0	70.2	54.5
nov0227	815.0	845.6	3.8	48.1	20.6
nov3008	813.1	847.9	−35.5	59.3	−0.4
nov3080	816.1	844.1	24.8	40.2	32.1
nov3083	814.0	842.0	−14.3	28.8	5.3
nov3113	818.6	851.2	59.8	75.1	55.8
nov3173	820.4	848.0	78.1	59.9	79.4

[a] cf, curve-fitting.

from Eq. (1) are typically closer to those of Eq. (3) than those from the DB2 single-peak calibration, Eq. (2). However, the DB2 single-peak calibration is more reliable for magnesian olivine compositions and the Fo values predicted by Eq. (2) are closer to the bulk of the data falling on the central curve. Eq. (2) gives a questionable (outstanding) estimate of Fo_{100} for only one spectrum—oct3503 from rock chip,476 (see Table 5). The S/N ratio of this doublet is one of the lowest in the data set ($\sim$2 for both peaks) and is plausibly in error. By using thought processes such as this we can make alternate Fo estimates of these data points and boost the number of useful data points. Here we have found reasonable estimates (falling within the range of the majority of the data) for 21 of the points scattering below the central curve and reduced the number of data points to be removed from the data set to one.

Two new pairs of histograms were created for the two rock chips; first after removing all of the data points that scatter more than $1.5\,cm^{-1}$ from the central curve (Fig. 13c) and then after substituting the DB2 single-peak estimates of the scattered data points for the Eq. (3) estimates (Fig. 13d). The ferroan tails of a and b are lacking in both, but Fig. 13c otherwise resembles Fig. 13b. In Fig. 13d the scattered data points have been largely consolidated into the Fo_{40-80} range and the relative bin populations slightly modified, but the character (unimodal vs. bimodal) of the histograms is unchanged. The degree of modification in the bin populations will depend on the proportion of scatted data points.

6. Conclusions

The two dominant Raman peaks of olivine form a doublet in the region 700–1100 cm^{-1} whose peak positions vary primarily as a function of $Mg/(Mg + Fe)$ and may be used to estimate the Fo content of the olivine. A tighter correlation was found between the DB2 peak positions (837.8–856.7 cm^{-1}) and Fo values for magnesian olivine ($Fo_{>50}$), making this peak the more reliable indicator of basaltic olivine compositions. However, a range of DB2 peak positions is observed in iron-rich olivine ($Fo_{<50}$—see Fig. 8b), so the DB1 (815.0–824.8 cm^{-1}) peak positions provide a better correlation to iron-rich olivine. A calibration that depends on both peaks of the olivine doublet was created to minimize errors across the spectrum of forsterite–fayalite compositions. This two-peak calibration achieves a similar accuracy as the DB2 single-peak calibration for intermediate and Mg-rich olivine compositions but overcomes its limitations for iron-rich olivine and is capable of predicting most olivine compositions to within ±10 Fo units.

Raman peaks from the two chemically zoned olivine samples used in the study are broader than those of the well-equilibrated samples and their Raman-derived Fo values scatter away from the regression lines of Figs. 6 and 10 more than those of the equilibrated samples. Compositional zoning is only a problem when it is

strong relative to the area excited by the laser beam ($\sim$6 μm diameter) in the Raman measurement. The most scatter we observed as the result of zoning is 1.5–2.0 wavenumbers away from the central median curve of the two-peak calibration (in LAP 02224,24). The discrepancies between the Raman-derived and EMP-derived Fo values are 10–11 Fo units for strongly zoned samples (e.g., zoned $\sim$2 Fo units within the diameter of the laser beam), but within 10 Fo units for weakly zoned samples (e.g., $\sim$0.4 Fo units within the diameter of the laser beam). The two compositionally zoned olivine samples help constrain the tolerance of the calibration when applied to zoned samples.

We applied the new two-peak calibration to the Raman point count data of Wang et al. (2004b). These spectra were taken on the rough rock surfaces of martian meteorite EETA 79001 without auto-focusing so the olivine doublets have variable S/N ratios. The Fo values derived from the two-peak calibration for the point count data (Fo_{50-85}) are in good agreement with Wang et al. (2004b) and previously published EMP data (Fo_{55-81}). Data points that scatter more than 1.5 wavenumbers below the central curve are from olivine doublets with low S/N ratios ($<$25 for both peaks) and produce low Fo estimates ($Fo_{<50}$) that are in error. If the data set is substantial, we recommend removing data points that have low S/N ratios and scatter $>$1.5 cm^{-1} above or below the median curve (data from our strongly zoned sample, LAP, scattered less than this) before making any petrographic interpretations. The single-peak calibrations may be used to revise the Fo estimates of these data points, and are probably best interpreted in the context of other minerals that constitute the assemblage.

Appendix A

Fayalite 203 and Forsterite 204. The synthetic end members, Fayalite 203 and Forsterite 204, are two of the standards used in the electron microprobe facility at Washington University. Fayalite 203 (Fo_{01}) is a dark, synthetic grain several millimeters across (Takei, 1978), grown in a lamp furnace heated to 1180° $\pm$ 5 °C under a con-

trolled CO_2–H_2–N_2 atmosphere and cooled at 400 °C/h. Forsterite 204 (Fo_{100}) is a synthetic, pale, green olivine that is several millimeters in diameter (Takei and Kobayashi, 1974). This grain was grown under a continuous N_2 gas flow (congruent melting at 1890 °C) and cooled at >300 °C/h. Synthetic forsterite crystals grown by Takei have been used in previous Raman studies of olivine (Ishii, 1978; Guyot et al., 1986).

Forsyth iron mine. The Forsyth Iron mine occurs in a Grenvillian metamorphic sequence. The main ore is magnetite, but hematite is also present along with iron-bearing silicates such as fayalite, hypersthene, augite, grunerite, and almandine (Hogarth, 1983). The fayalite is coarse-grained (Fo_{08}) and anhedral with veins of magnetite (Jambor et al., 2002; purchased from Wards). All spectra were acquired in areas away from the veins but both spectra used in the calibration contain minor magnetite peaks.

Hortonolite. This sample is from Rustenburg, South Africa, has a composition of Fo_{41} and was obtained from the Harvard University mineral collection (#118652). The sample likely comes from (or is related to) the rocks of the Rustenburg Mine, Rustenburg District, Western Bushveld Complex, Northwest Province, South Africa. Wilson et al. (1999) note that olivine-rich rocks occur in the footwall sequences of the Union and Amandelbult mines in the northwest portion of the Rustenburg layered suite. This sample also contains veins of magnetite but these are thinner than those of the Forsyth sample. Again, the spectra used in the calibration were acquired away from the veins but magnetite peaks still appear in a few spectra. Sunshine and Pieters (1998) report a wet chemical (bulk) analysis for a Rustenburg olivine (same Harvard number) with ~3.8 wt% Fe_2O_3.

Twin Sisters dunite. The Twin Sisters is a dunite massif (Fo_{90-92}, with minor harzburgite), exposed in the western portion of the Cascade Mountains of Washington State (Christensen, 2002). The dunite is porphyroclastic in texture; the olivine grains have a size range from 0.1 mm to >2 cm and are strained and flattened with petrofabrics characteristic of high temperatures and low strain (Christensen, 2002). Sunshine and Pieters (1998) used samples from the Twin Sisters massif in their study of olivine reflectance spectra.

Northwest Africa (NWA) 773. NWA 773 is a brecciated lunar meteorite that contains a prominent olivine-gabbro cumulate lithology (Fagan et al., 2003; Jolliff et al., 2003) and a polymict breccia lithology. Only the mm sized, subhedral to euhedral olivine grains in the cumulate lithology are used in the present study. These olivine grains are equilibrated and have compositions in the range of Fo_{64-70}. The olivine-gabbro cumulate lithology is interpreted as a shallow intrusive on the basis of texture and mineral chemistry (Jolliff et al., 2003). Because this meteorite resided in a hot desert environment on Earth, it contains intergranular deposits of calcite precipitated from the evaporation of ground moisture. The olivine grains within the meteorite are unaltered and all EMP and Raman analyses were ac-

quired in unfractured areas away from any calcite. However, calcite is commonly observed in the Raman spectra owing to the penetration of the laser beam to grain boundaries beneath the surface of the sample.

Elephant Moraine 79001,530, lithology A (EETA). EETA 79001 is a basaltic shergottite, one of the three classes of martian meteorites (S-N-C). Among the SNC meteorites, EETA is noted for containing two related igneous lithologies (A and B) whose contact is gradational in thin section and presumably igneous (Score and Reid, 1981; Meyer, 1996). Lithology A is strongly olivine-normative with a porphyritic texture containing composite megacrysts of olivine, orthopyroxene, and chromite. Lithology B is barely olivine normative and resembles the groundmass of lithology A; but is coarser grained and more evolved (McSween and Jarosewich, 1983). Only the olivine megacrysts in thin section,530 (made from one of the 4 pieces originally allocated to us as EETA 79001,482—taken from near the contact) were used in the calibration. These megacrysts have homogeneous cores but are zoned in their outer portions and rimmed with pigeonite, suggesting disequilibrium with the groundmass (McSween and Jarosewich, 1983). The published range of compositions for the olivine xenoliths is Fo_{55-80} (Steele and Smith, 1982; McSween and Jarosewich, 1983; Wang et al., 2004b).

Olivine spectra from four Raman point counts on one rock chip of EETA 79001,476 (lithology A) and from seven traverses on four chips of EETA 79001,482 (taken from an area near the contact between lithologies A and B) demonstrate the use of the calibration with a lower signal-to-noise data set similar to that anticipated from field measurements. The laser was focused only at the beginning of the traverses so that subsequent analyses are slightly out of focus, with an estimated surface relief of ~1 mm (see Wang et al., 2004b for full experimental details).

San Carlos. The San Carlos volcanic field occurs in SE Arizona on Peridot Mesa, a Late Tertiary to Quaternary basanite flow about 30 km east of Globe, AZ (Frey and Prinz, 1978; Galer and O'nions, 1989). Ultramafic materials (Fo_{91}) are exposed in Peridot Canyon on the San Carlos Indian Reservation (Frey and Prinz, 1978) where they comprise >50% (by volume) of the lower parts of the flow. The San Carlos is noted for containing large, gem-quality peridot. Our sample is an individual, polished olivine crystal several mm in diameter that lacks inclusions. Guyot et al. (1986) used Raman spectra of San Carlos olivine in their comparison of olivine and spinel structures and Sunshine and Pieters (1998) used a San Carlos sample in their study of olivine reflectance spectra.

La Paz Hills 02224,24 (LAP). This sample is a lunar meteorite and was collected from the La Paz Ice field in Antarctica (McBride et al., 2003, 2004a,b). It is a subophitic, low-Ti mare basalt dominated by pyroxene and plagioclase with minor olivine (modal abundance ~3%) and ilmenite. Olivine of both fayalitic (Fo_{1-5}) and intermediate compositions are present (cores of Fo_{55-65} and rims rang-

ing from Fo_{20} to Fo_{45}, Zeigler et al., 2005). The olivine grains range up to 1 mm in size, are anhedral, and some contain chromite and/or Cr-ulvöspinel inclusions. The fayalite grains contain ~0.8 wt% CaO and give anomalously low Raman peak positions. Thus they were not used in this study. The olivine with intermediate compositions are substantially zoned (our EMP analyses indicate zoning of 20 Fo units within 75 μm) and were also omitted from the data set used to develop the calibration equations; but are included with the full data set to evaluate the accuracy of the calibration with zoned olivine.

Finch-Robie. This is a synthetic fayalite loaned to us by Anne Hofmeister, this is the same olivine grain used in the single-crystal IR study of Hofmeister (1987) and the single-crystal Raman study of Chopelas (1991). This sample was originally described by Finch et al. (1980) who note that it contains between 0.27 and 0.86% Fe^{3+}. No EMPA data are available so it was not used in generating or testing the calibration but is referred to in the discussion of the calibration.

References

Armstrong, J.T., 1988. Quantitative analysis of silicate and oxide materials: comparison of Monte Carlo, ZAF, and $\phi(\rho Z)$ procedures. *Microbeam Anal.* **23**, 239–245.

Bridges, J.C., Jeffries, T.E., Grady, M.M., 2002. Trace element signatures of trapped KREEP in olivine-rich clasts within lunar meteorite NWA 773, abstract #5137, *Meteor. Planet. Sci.* **37**, No. 7 (Suppl.), A24.

Burns, R.G., Huggins, F.E., 1972. Cation determinative curves for Fe–Mg–Mn olivine from vibrational spectra. *Am. Mineral.* **57**, 967–985.

Chopelas, A., 1991. Single crystal Raman spectra of forsterite, fayalite, and monticellite. *Am. Mineral.* **76**, 1101–1109.

Christensen, N.I., 2002. Continental mantle seismic anisotropy: A new look at the Twin Sisters massif. *Tectonophysics* **355**, 163–170.

Cooney, T.F., Sharma, S.K., 1990. Structure of glasses in the systems Mg_2SiO_4–Fe_2SiO_4, $MnSiO_4$–Fe_2SiO_4, Mg_2SiO_4–$CaMgSiO_4$, and Mn_2SiO_4–$CaMnSiO_4$. *J. Non-Cryst. Solids* **122**, 10–32.

Deer, W.A., Howie, R.A., Zussman, J., 1992. *The Rock Forming Minerals*, second ed. Pearson Education Unlimited, Harlow, England, pp. 3–13.

Dyar, M.D., Delaney, J.S., Sutton, S.R., Schaeffer, M.W., 1998. Fe^{3+} distribution in oxidized olivine: a synchrotron micro-XANES study. *Am. Mineral.* **83**, 1361–1365.

Fagan, T., Taylor, G.J., Keil, K., Hicks, T.L., Killgore, M., Bunch, T.E., Wittke, J.H., Mittlefehldt, D.W., Clayton, R.N., Mayeda, T., Eugster, O., Lorenzetti, S., Norman, M.D., 2003. Northwest Africa 773: Lunar origin and iron-enrichment trend. *Meteor. Planet. Sci.* **38**, 529–554.

Finch, C.B., Clark, G.W., Kopp, O., 1980. Czochralski growth of single-crystal fayalite under controlled oxygen fugacity conditions. *Am. Mineral.* **65**, 381–389.

Freeman, J.J., Wang, A., Kuebler, K., Haskin, L.A., 2003. Raman spectroscopic characterization of feldspars—Implications for in-situ surface mineral characterization in planetary exploration. Lunar Planet. Sci. Conf. XXXIV, #1676.

Frey, F., Prinz, M., 1978. Ultramafic Inclusions from San Carlos, Arizona: Petrologic and geochemical data bearing on their petrogenesis. *Earth Planet. Sci. Lett.* **38**, 129–176.

Galer, S.J.G., O'nions, R.K., 1989. Chemical and isotopic studies of ultramafic inclusions from the San Carlos volcanic field, Arizona: a bearing on their petrogenesis. *J. Petrol.* **30** (4), 1033–1064.

Guyot, F., Boyer, H., Madon, M., Velde, B., Poirer, J.P., 1986. Comparison of the Raman microprobe spectra of $(Mg,Fe)_2SiO_4$ and Mg_2GeO_4 with olivine and spinel structures. *Phys. Chem. Mineral.* **13**, 91–95.

Haskin, L.A., Wang, A., Rockow, K.M., Jolliff, B.L., Korotev, R.L., Viskupic, K.M., 1997. Raman spectroscopy for mineral identification and quantification for in situ planetary surface analysis: a point count method. *J. Geophys. Res.* **102**, 19293–19306.

Hofmeister, A., 1987. Single-crystal absorption and reflection infrared spectroscopy of forsterite and fayalite. *Phys. Chem. Mineral.* **13**, 91–95.

Hofmeister, A., Chopelas, A., 1991. Vibrational spectroscopy of end-member silicate garnets. *Phys. Chem. Mineral.* **13**, 503–526.

Hogarth, D.D., 1983. The Hull iron range: 1801–1977. *Can. Inst. Min. (CIM) Bull.* **76**, 854, 75-84.

Ishii, K., 1978. Lattice dynamics of forsterite. *Am. Mineral.* **63**, 1198–1208.

Ishii, K., Torigoe, K., Han, X.J., 1997. Oriented precipitate complexes in iron-rich olivines produced experimentally in aqueous oxidizing environment. *Phys. Chem. Mineral.* **25**, 8–14.

Jambor, J.J., Dutrizac, J.E., Groat, L.A., Raudsepp, M., 2002. Static tests of neutralization potentials of silicate and aluminosilicate minerals. *Environ. Geol.* **43**, 1–17.

Jolliff, B.L., Korotev, R.L., Zeigler, R.A., Floss, C., 2003. Northwest Africa 773: Lunar mare breccia with a shallow-formed olivine-cumulate component, inferred very-low-Ti (VLT) heritage, and a KREEP connection. *Geochim. Cosmochim. Acta* **67** (24), 4857–4879.

Khisina, N.R., Khramov, D.A., Kolosov, M.V., Kleschev, A.A., Taylor, L.A., 1995. Formation of ferriolivine and magnesioferrite in Mg-Fe olivine. *Phys. Chem. Mineral.* **22**, 241–250.

Kitamura, M., Shen, B., Banno, S., Morimoto, N., 1984. Fine textures of laihunite, a nonstoichiometric disoriented olivine-type material. *Am. Mineral.* **69**, 154–160.

Korotev, R.L., Zeigler, R.A., Jolliff, B.L., Haskin, L.A., 2002. Northwest Africa 773—An unusual rock from the lunar maria, abstract #5259. *Meteor. Planet. Sci.* **37**, No. 7 (Suppl.), A81.

Kuebler, K., Jolliff, B.L., Wang, A., Haskin, L.A., 2002. A Raman spectroscopic study of samples from the May 2001 FIDO test site. *Lunar Planet. Sci. Conf.* XXXIII, #1536.

Lam, P., Yu, R., Lee, M.W., Sharma, S., 1990. Structural distortions and vibrational modes in Mg_2SiO_4. *Am. Mineral.* **75**, 109–119.

McBride, K., McCoy, T., Welzenbach, L., 2003. LAP 02205. In: Satterwhite, C., Righter, K. (Eds.), *Ant. Met. News.* **26** (2).

McBride, K., McCoy, T., Welzenbach, L., 2004a. LAP 02224, 02226, and 02436. In: Satterwhite, C., Righter, K. (Eds.), *Ant. Met. News.* **27** (1).

McBride, K., McCoy, T., Welzenbach, L., 2004b. LAP 003632. In: Satterwhite, C., Righter, K. (Eds.), *Ant. Met. News.* **27** (3).

McMillan, P., 1985. Vibrational spectroscopy in the mineral sciences. In: Kieffer, S.W., Navrotsky, A. (Eds.), *Microscopic to Macroscopic*. Reviews in Mineralogy, vol. 14, Mineralogical Society of America, Washington.

McSween, H.Y., Jarosewich, E., 1983. Petrogenesis of the Elephant Moraine A79001 meteorite: multiple magma pulses on the shergottite parent body. *Geochim. Cosmochim. Acta* **47**, 1501–1513.

Mernagh, T.P., Hoatson, D.M., 1997. Raman spectroscopic study of pyroxene structures from the Munni Munni Layered Intrusion, Western Australia. *J. Raman Spectrosc.* **28**, 647–658.

Meyer, C., 1996. *Mars Meteorite Compendium*. JSC Report 27672. Johnson Space Center, Houston, TX, pp. 43–50, 67–90. (Also available at: <http://www-curator.jsc.nasa.gov/curator/antmet/mmc/mmc.htm/>).

Mohanan, K., Sharma, S.K., Bishop, F.C., 1993. A Raman spectral study of forsterite-monticellite solid solutions. *Am. Mineral.* **78**, 42–48.

Papike, J.J., 1987. Chemistry of the rock-forming silicates: ortho, ring, and single-chain structures. *Rev. Geophys.* **25** (7), 1483–1526.

Pàques-Ledent and Tarte, M.T., Tarte, P., 1973. Vibrational studies of olivine-type compounds –I. The i.r. and Raman spectra of the isotopic species of Mg_2SiO_4. *Spectrochim. Acta* **29A**, 1007–1016.

Piriou, B., McMillan, P., 1983. The high-frequency vibrational spectra of vitreous and crystalline orthosilicates. *Am. Mineral.* **68**, 426–443.

Price, G.D., Parker, S.C., Leslie, M., 1987. The lattice dynamics of forsterite. *Mineral. Mag.* **51**, 157.

Score, R., Reid, A., 1981. Physical and petrographic description of EETA 79001. In: *Ant. Met. News*, vol. 4. No. 1. Johnson Space Center Publication, Houston, p. 133.

Smith, D.C., 2005. The RAMANITA method for non-destructive and in-situ semi-quantitative chemical analysis of mineral solid-solutions by multi-dimensional calibration of Raman wavenumber shifts. *Spectrochim. Acta* **A61**, 2299–2314.

Smyth, J.R., Bish, D.L., 1988. *Crystal Structures and Cation Sites of the Rock Forming Minerals*. Allen & Unwin, Boston.

Steele, I.M., Smith, J.V., 1982. Petrography and mineralogy of two basalts and olivine-pyroxene-spinel fragments in achondrite EETA 79001. In: Proceedings of the 13th Lunar Planetary Science Conference, pp. A375–A384.

Sunshine, J.M., Pieters, C., 1998. Determining the composition of olivine from reflectance spectroscopy. *J. Geophys. Res.* **103** (E6), 13675–13688.

Takei, H., 1978. Growth of fayalite (Fe_2SiO_4) single crystals by the floating zone method. *J. Cryst. Growth* **43**, 463–468.

Takei, H., Kobayashi, T., 1974. Growth and properties of Mg_2SiO_4 single crystals. *J. Cryst. Growth* **23**, 121–124.

Wang, A., Jolliff, B.L., Haskin, L.A., 1995. Raman spectroscopy as a method for mineral identification on lunar robotic exploration missions. *J. Geophys. Res.* **100**, 21189–21199.

Wang, A., Jolliff, B.L., Haskin, L.A., 1999. Raman spectroscopic characterization of a highly weathered basalt: igneous mineralogy, alteration products, and a microorganism. *J. Geophys. Res.* **104** (E11), 27067–27077.

Wang, A., Jolliff, B.L., Haskin, L.A., Kuebler, K.E., Viskupic, K.M., 2001. Characterization and comparison of structural and compositional features of planetary quadrilateral pyroxenes by Raman spectroscopy. *Am. Mineral.* **86**, 790–806.

Wang, A., Jolliff, B.L., Haskin, L.A., 2003a. Investigating surface mineralogy, alteration processes, and biomarkers on Mars using laser Raman spectroscopy. In: *6th International Conference on Mars*, #3270. <http://www.lpi.usra.edu/meetings/sixthmars2003/pdf/3270.pdf/>.

Wang, A., Haskin, L.A., Lane, A.L., Wdowiak, T.J., Squyers, S.W., Wilson, R.J., Hovland, L.E., Manatt, K.S., Raouf, N., Smith, C.D., 2003b. Development of the Mars Microbeam Raman Spectrometer (MMRS). *J. Geophys. Res.* **108** (E1), 5005. doi:10.1029/2002JE001902.

Wang, A., Kuebler, K.E., Jolliff, B.L., Haskin, L.A., 2004a. Raman spectroscopy of Fe–Ti–Cr oxides, case study: martian meteorite EETA 79001. *Am. Mineral.* **89**, 665–680.

Wang, A., Kuebler, K., Jolliff, B.L., Haskin, L.A., 2004b. Mineralogy of a Martian meteorite as determined by Raman spectroscopy. *J. Raman Spectrosc.* **35**, 504–514.

Wang, A., Freeman, J., Greenhagen, B., Jolliff, B., 2005. Raman spectra of hydrated Mg- and Ca-sulfates and field testing the Mars Microbeam Raman Spectrometer (MMRS) [abstract]. *Geol. Soc. Am. Abstr. Prog.* **37** (7), 55.

Whittaker, E.J.W., Muntus, R., 1970. Ionic radii for use in geochemistry. *Geochim. Cosmochim. Acta* **34**, 945–956.

Wilson, A.H., Lee, C.A., Brown, R.T., 1999. Geochemistry of the Merensky Reef, Rustenburg Section, Bushveld Complex: controls on the silicate framework and distribution of trace elements. *Miner. Deposita* **34**, 657–672.

Zeigler, R.A., Korotev, R.L., Jolliff, B.L., Haskin, L.A., 2005. Petrography and geochemistry of the LaPaz Icefield basaltic lunar meteorite and source-crater pairing with Northwest Africa 032. *Meteor. Planet. Sci.* **40** (7), 1073–1101.